Astrocytic neogenin/netrin-1 pathway promotes blood vessel homeostasis and function in mouse cortex

Ling-Ling Yao,[1,2] Jin-Xia Hu,[2,3] Qiang Li,[2,4] Daehoon Lee,[1] Xiao Ren,[1,5] Jun-Shi Zhang,[1,6] Dong Sun,[1,2] Hong-Sheng Zhang,[1,2] Yong-Gang Wang,[5] Lin Mei,[1,2] and Wen-Cheng Xiong[1,2]

[1]Department of Neurosciences, School of Medicine, Case Western Reserve University, Cleveland, Ohio, USA. [2]Department of Neuroscience and Regenerative Medicine, Medical College of Georgia, Augusta University, Augusta, Georgia, USA. [3]Institute of Stroke Center and Department of Neurology, Xuzhou Medical University, The Affiliated Hospital of Xuzhou Medical University, Jiangsu, China. [4]Department of Hand Surgery, China-Japan Union Hospital, Jilin University, Changchun, China. [5]Beijing Tiantan Hospital, Capital Medical University, Beijing, China. [6]Department of Neurology, Huaihe Hospital, Henan University, Kaifeng, Henan, China.

Astrocytes have multiple functions in the brain, including affecting blood vessel (BV) homeostasis and function. However, the underlying mechanisms remain elusive. Here, we provide evidence that astrocytic neogenin (NEO1), a member of deleted in colorectal cancer (DCC) family netrin receptors, is involved in blood vessel homeostasis and function. Mice with Neo1 depletion in astrocytes exhibited clustered astrocyte distribution and increased BVs in their cortices. These BVs were leaky, with reduced blood flow, disrupted vascular basement membranes (vBMs), decreased pericytes, impaired endothelial cell (EC) barrier, and elevated tip EC proliferation. Increased proliferation was also detected in cultured ECs exposed to the conditioned medium (CM) of NEO1-depleted astrocytes. Further screening for angiogenetic factors in the CM identified netrin-1 (NTN1), whose expression was decreased in NEO1-depleted cortical astrocytes. Adding NTN1 into the CM of NEO1-depleted astrocytes attenuated EC proliferation. Expressing NTN1 in NEO1 mutant cortical astrocytes ameliorated phenotypes in blood-brain barrier (BBB), EC, and astrocyte distribution. NTN1 depletion in astrocytes resulted in BV/BBB deficits in the cortex similar to those in Neo1 mutant mice. In aggregate, these results uncovered an unrecognized pathway, astrocytic NEO1 to NTN1, not only regulating astrocyte distribution, but also promoting cortical BV homeostasis and function.

Introduction

The brain, the organ that consumes the most energy, depends on a cerebral blood supply to obtain oxygen and nutrients for neuronal function. Malformation or dysfunction of blood vessels (BVs) in the brain results in altered blood flow and impaired cognitive function, which are implicated in multiple neurological diseases, including Moyamoya disease, small vessel disease (SVD), and Alzheimer's disease (AD) (1). BVs in the brain consist of interconnected arteries, capillaries, and veins, which all contain endothelial cells (ECs) and supporting cells. Whereas smooth muscle cell is a supporting cell for arteries, pericytes support capillaries and veins (2, 3). In addition, astrocytes, a major type of glial cells, are also considered BV-supporting cells. BVs in adult brain are highly dynamic, undergoing angiogenesis and/or pruning. Thus, it is of considerable interest to investigate how BV remodeling, homeostasis, and function are regulated.

Astrocytes play multiple regulatory roles in the development and function of BV and the blood-brain barrier (BBB) (4). They are necessary for BV/BBB remodeling and homeostasis in the cortex (5, 6). They bridge neuronal activity to regulate local blood flow, link the metabolic substances of active neurons and glial cells to control arteriole contraction and dilation, and communicate with pericytes for capillary BBB regulation (5). Whereas astrocytes' roles in BV/BBB development and function are evident, the underlying mechanisms and astrocytic functions in BV remodeling and homeostasis remain to be elucidated.

Astrocytes' regulation of BV/BBB development and function is likely accomplished in 2 ways: direct interaction with BVs (ECs and pericytes) and secretion of growth factors and/or extracellular matrix proteins important for angiogenesis/BV pruning and BBB (3). While acute depletion of the astrocyte-BV interaction site (endfeet) by laser ablation results in little effect on the recovery of BBB function (6), a growing number of astrocyte-derived extracellular proteins that regulate brain angiogenesis have been identified; these include VEGF, TGF-β, bone morphogenesis proteins (BMP), Wnt7, ephrins, semaphorins, slits, and netrins (7–12). Among these factors, netrin-1 (NTN1), which was initially identified as an axon guidance cue, is noteworthy (8, 9). Similar to NTN1's function in axon guidance, playing both attractive and repulsive roles, is its reported role as a pro- or antiangiogenic factor, which is likely due to NTN1's complex receptor family members, including deleted in colorectal cancer (DCC) and UNC5 family members (10–13). NTN1 suppresses EC tip cell migration and angiogenesis during development, which is likely due to its receptor UNC5B (12). NTN1 has also been found to promote angiogenesis by stabilizing vessels (10–13). Recently, cluster of differentiation 146 (CD146),

Authorship note: LLY, JXH, and QL contributed equally to this work.
Conflict of interest: The authors have declared that no conflict of interest exists.

Submitted: August 6, 2019; **Accepted:** August 20, 2020;
Published: November 3, 2020.
Reference information: *J Clin Invest*. 2020;130(12):6490–6509.
https://doi.org/10.1172/JCI132372.

also known as the melanoma cell adhesion molecular (MCAM) or cell surface glycoprotein MUC18, has been suggested as mediating NTN1's proangiogenesis effect (10, 11). However, the role of DCC family NTN1 receptors in BV development and function in the brain remains largely unknown.

Neogenin (NEO1), a DCC family receptor for netrins (14), is abundantly expressed in astrocytes in addition to neural stem cells (NSCs), oligodendrocytes, and neurons in the brain (15). Although NEO1 was initially identified as an NTN1 receptor, its role in NTN1-regulated axonal guidance remains unidentified (15, 16). The NEO1 hypomorphic allele results in multiple phenotypes, including early neonatal death, neonatal hydrocephalus (17), and olfactory neuron migration deficit (18). Investigating NEO1's function in NSCs by the use of its conditional KO mouse models has demonstrated NEO1's functions in promoting neocortical astrogliogenesis (19) and adult hippocampal neurogenesis (20). However, NEO1's role in astrocytes and/or in BV/BBB development and function remains unexplored.

Here, we report astrocytic NEO1's function in regulating BV remodeling, homeostasis, and BBB function in mouse cortex. Astrocyte-specific, but not pyramidal neuron–specific, Neo1-KO cortex exhibited smaller arterioles, more veins and capillaries, which had reduced blood flow, impaired vascular basement membranes (vBMs), fewer pericytes, increased EC caveolae and EC fenestrae, and leaky BBBs. These vessel phenotypes appeared to be brain-region selective, obviously in the mutant somatosensory cortex, but were undetectable in the hippocampus or retina. Additionally, Neo1-KO astrocytes displayed an altered and clustered distribution pattern. Moreover, NEO1 KO impaired BMP2 induction of NTN1 expression in cortical astrocytes and NTN1 played essential roles not only in suppressing tip EC proliferation and angiogenesis, but also in maintaining vBM and pericytes. In aggregate, these results uncover an unrecognized pathway, astrocytic NEO1 to NTN1, in regulating astrocyte distribution, suppressing tip cell proliferation, and promoting vBM organization, revealing a mechanism underlying astrocyte regulation of cortical BV/BBB homeostasis and function.

Results

Reduced DiI$^+$ BV, but increased PECAM-1$^+$ BV density, in Neo1-KO cortex. To investigate NEO1's function in mouse brain, we generated a conditional Neo1-KO mouse line, *Neo*$^{GFAP\text{-}Cre}$, in which the floxed NEO1 (*Neo*$^{fl/fl}$) allele was crossed with the hGFAP promoter driven Cre mouse, as described previously (19, 21). The *hGFAP-Cre* mouse line expresses Cre not only in astrocytes, but also in radial glial cells (RGCs), NSCs, and their progenies (22). In our initial examination of the mouse brain structures, the mutant brain tissues were not well fixed with a standard in vivo perfusion method (injection of PBS buffer containing 4% paraformaldehyde [PFA] into left ventricle of anesthetized mice; see details in Methods). However, the mutant brain sections could be fixed with the same buffer in vitro. We thus speculate that there is a defective PFA buffer flow from the peripheral BVs to the mutant brain during in vivo perfusion. To test this speculation, the perfusion method was modified by adding DiI into the perfusion buffer because DiI binds to BV ECs and fluorescently labels BVs and thus could serve as a reporter for both perfusion buffer flow and BVs in the brain (23) (Figure 1A). Indeed, DiI$^+$ vessels appeared at a lower rate in the mutant cortex than in those of littermate controls (at P60) (Figure 1, B and C). We then asked whether the reduced DiI$^+$ BVs in the mutant cortex could result from reduced BVs and/or abnormal BV blockage of DiI PFA buffer flow. To this end, the brain sections from DiI PFA–perfused control and mutant mice were refixed with 4% PFA buffer in vitro and then subjected to immunostaining analysis using antibody against PECAM-1 (also called CD31), a marker of BV ECs (24). The PECAM-1$^+$ vessels in the mutant cortex were not less but were more abundant than those of controls (Figure 1, B, D–F). Quantification analyses showed significant elevations in the total length and branch points of PECAM-1$^+$ vessels in the mutant cortex (Figure 1, D–F). These results thus eliminate the possibility of reduced BVs, implicate a deficit in perfusion buffer flow in the mutant cortex, and suggest a role of NEO1 in regulating cortical BV morphogenesis and function.

Similar vessel deficit in astrocyte-specific, but not pyramidal neuron–specific, Neo1-KO cortex. NEO1 is expressed in multiple types of brain cells, including astrocytes (15), NSCs (25), and neurons (26). *Neo*$^{GFAP\text{-}Cre}$ mice are likely to abolish its expression in all these cell types (27). To determine in which brain cell type(s) NEO1 plays an important role for BV morphogenesis and function, we generated additional Neo1-CKO mouse lines(where CKO indicates conditional KO), *Neo*$^{GFAP\text{-}CreER}$ and *Neo*$^{Nex\text{-}Cre}$, in which *Neo*$^{fl/fl}$ mice were crossed with *GFAP-CreER* and *Nex-Cre* mice, respectively (Supplemental Figure 1, A and B; supplemental material available online with this article; https://doi.org/10.1172/JCI132372DS1). In *GFAP-CreER* mice, upon tamoxifen (TAM) treatment (100 mg/kg/d, once/d for 4 days), Cre was active specifically in astrocytes (Supplemental Figure 1, F–H), and thus NEO1 was selectively knocked out in astrocytes in *Neo*$^{GFAP\text{-}CreER}$ mice (Supplemental Figure 1, A, C–E). *Nex-Cre* mice express Cre in pyramidal neurons starting at E11.5 (28), and thus NEO1 was specifically knocked out in pyramidal neurons in *Neo*$^{Nex\text{-}Cre}$ mice (Supplemental Figure 1, B, D, and E). Approximately 68% and 25% of NEO1 was depleted in cortices from *Neo*$^{GFAP\text{-}CreER}$ and *Neo*$^{Nex\text{-}Cre}$ mice, respectively (Supplemental Figure 1, D and E), supporting the view that NEO1 is largely expressed in astrocytes.

As illustrated in Figure 1A, *Neo*$^{GFAP\text{-}CreER}$ and their control mice (*GFAP-CreER* and *Neo*$^{fl/fl}$) were injected with TAM at P30, and at P60, these mice as well as *Neo*$^{Nex\text{-}Cre}$ mice were perfused with 4% PFA DiI buffer and their brain sections were refixed with 4% PFA buffer and subjected to immunostaining analysis. Interestingly, DiI$^+$ BVs in the cortex of *Neo*$^{GFAP\text{-}CreER}$, but not *Neo*$^{Nex\text{-}Cre}$, mice were reduced, but PECAM-1$^+$ BV density was increased (Figure 1, G–L), so that these mice exhibited vessel phenotypes similar to those of *Neo*$^{GFAP\text{-}Cre}$ mice, suggesting the function of astrocytic NEO1 in this event. Notice that these vessel phenotypes were obvious in the mutant cerebral cortex, in particular the somatosensory cortex, but not the hippocampus or retina as compared with their controls (*Neo*$^{fl/fl}$ and *GFAP-CreER*) (Supplemental Figure 2), indicating a brain-regional selectivity. Together, these results suggest that astrocytic NEO1 plays a critical role in cortical BV homeostasis and function.

Reduced blood flow, but increased BBB leakage, in the Neo$^{GFAP\text{-}CreER}$ *cortex*. To further determine whether the reduced DiI$^+$ BVs in the mutant cortex are due to a defective DiI buffer or blood

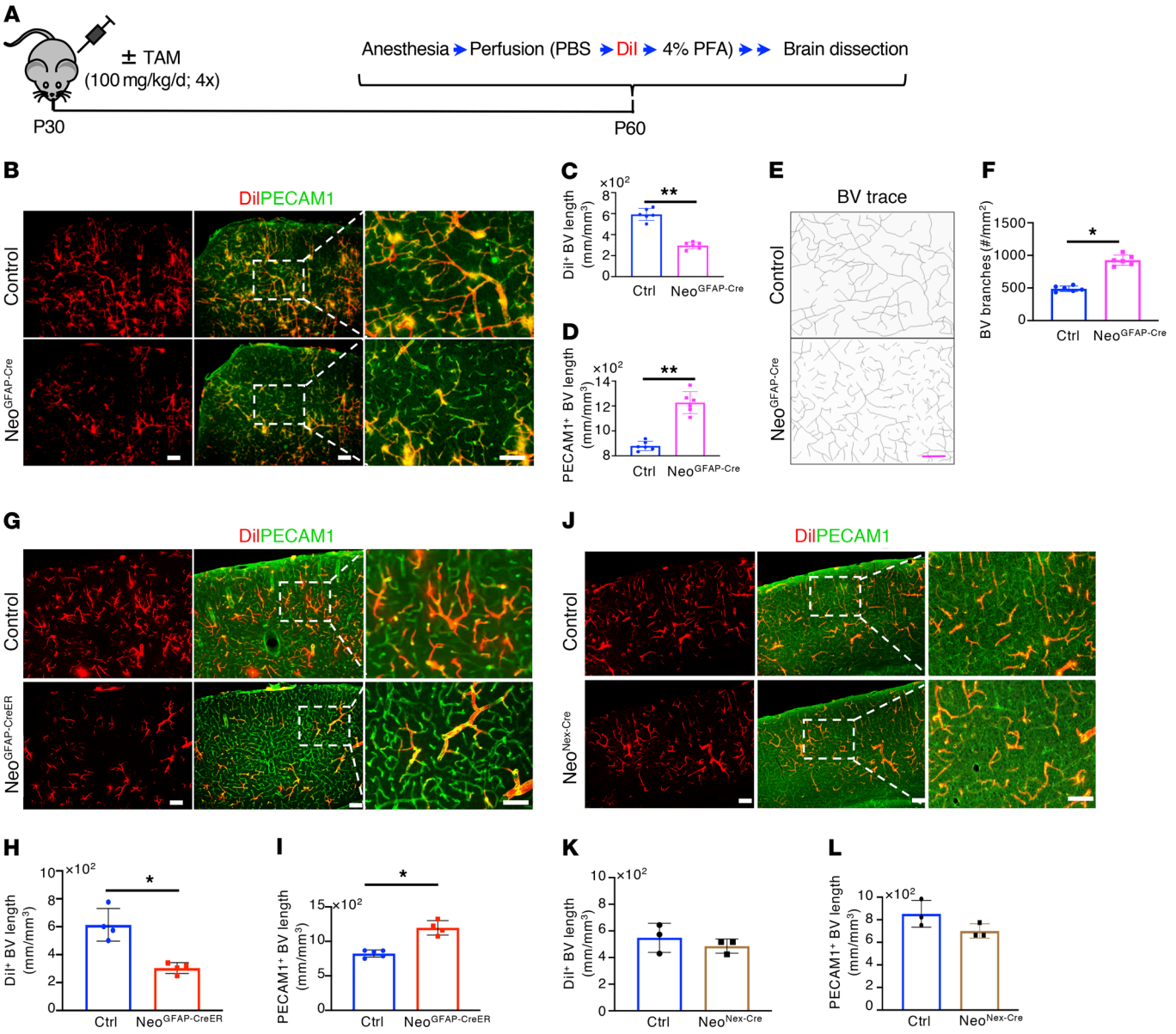

Figure 1. Reduced DiI⁺ vessels, but increased PECAM-1⁺ vessels, in astrocytic, but not pyramidal neuronal, Neo1-KO cortex. (**A**) Schematic of the protocol for DiI perfusion. (**B**) Representative images of BVs in the cortex of control (*Neo*$^{fl/fl}$) and *Neo*$^{GFAP\text{-}Cre}$ mice (at P60). Brain sections were subjected to immunostaining analysis using antibodies against PECAM-1 (green). Images were captured from 6 slides per animal. Average number of DiI⁺ vessel length per cubic millimeters was calculated and is presented in **C**, and PECAM-1⁺ vessel length was quantified and is presented in **D**. BV tracing and quantification of BV branches are shown in **E** and **F**, respectively. (**G**) Representative images of BVs in cortices of littermate control *Neo*$^{fl/fl}$ and *Neo*$^{GFAP\text{-}CreER}$ mice. Mice were injected with TAM at P30 and perfused with DiI at P60 before sacrifice. (**H** and **I**) Quantitative analyses of data in **G**. (**J**) Representative images of BVs in cortices of littermate control and *Neo*$^{Nex\text{-}cre}$ mice at P60. (**K** and **L**) Quantitative analyses of data in **J**. Scale bars: 50 μm. Data are represented as mean ± SEM (n = 3 to 6 mice/group). *P < 0.05; **P < 0.01, Mann-Whitney U statistical test.

flow from the peripheral BVs to their cortex, we used laser Doppler to measure blood flow in the control and mutant cortices. Control and *Neo*$^{GFAP\text{-}CreER}$ mice were anesthetized, and their skull skins (~1.76 cm^2) were opened and subjected to laser Doppler scanning and imaging analysis. As shown in Figure 2, A and B, blood flow was indeed less in the *Neo*$^{GFAP\text{-}CreER}$ cortex than in that of control mice, supporting this view.

We then asked whether the flow of tail-vein–injected Evans blue (EB) (which binds to albumin with red fluorescence) or green fluorescent–labeled dextrans (MW 10 kDa and 3 kDa) were also reduced in the mutant cortex and whether BBB in the mutant cortex could be examined by this assay. The EB or dextran was injected into the tail veins of live *Neo*$^{GFAP\text{-}CreER}$ mutant and control mice (*Neo*$^{fl/fl}$ and *GFAP-CreER*) (without anesthesia by 3% isoflurane) (see Figure 2C). Thirty minutes after, mice were anesthetized and perfused with PBS and 4% PFA (see Figure 2C). Their brain sections were post-fixed in vitro and subjected to immunostaining analysis. Little to no EB⁺ or dextran⁺ signals were detected in control brain sections. In contrast, both EB⁺ and dextran⁺ signals were observed in the mutant cortex (Figure 2, D–I). Confocal

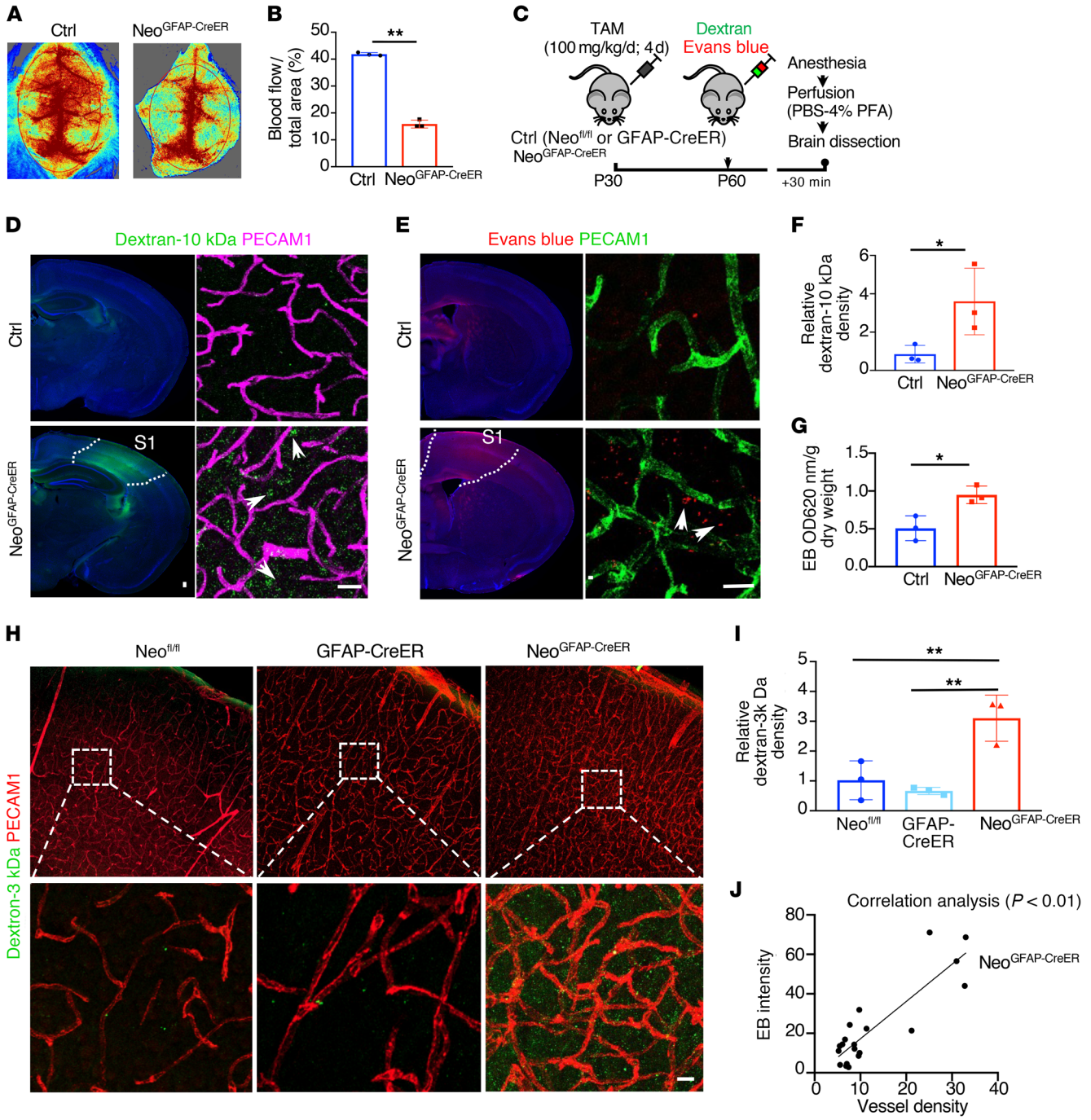

Figure 2. Reduced blood flow, but increased BBB leakage, in *Neo*$^{GFAP\text{-}CreER}$ cortex. (**A**) Representative images and (**B**) quantification of laser Doppler measurement of blood flow signals in control (*Neo*$^{fl/fl}$) and *Neo*$^{GFAP\text{-}CreER}$ cortices (TAM at P30, imaged at P60). (**C**) Schematic of the protocol for EB and dextran injections. (**D** and **E**) Representative images of 10 kDa dextran (green) and EB (red) coimmunostained with anti-PECAM-1 in P60 control (*neo*$^{fl/fl}$) and *Neo*$^{GFAP\text{-}CreER}$ cortex. (**F**) Quantitative analysis of data in **D**. (**G**) Quantitative analysis of EB extravasation. (**H** and **I**) Representative images of immunostaining using indicated antibodies (**H**) and the quantification (**I**) of 3 kDa dextran (green) in control (*neo*$^{fl/fl}$ and *GFAP-CreER*) and *Neo*$^{GFAP\text{-}CreER}$ cortex. (**J**) Pearson's analysis of the correlation between EB leakage and vessel density in *Neo*$^{GFAP\text{-}CreER}$ cortex. Scale bars: 20 μm. Data are represented as mean ± SEM (n = 3 mice/group). *P < 0.05; **P < 0.01, Student's t test (**B**, **F**, and **G**); 1-way ANOVA plus post hoc analysis (**I**).

imaging analysis showed EB$^+$ and dextran$^+$ signals largely on the outside of PECAM-1$^+$ BVs in the mutant cortex (Figure 2, D and E). These results suggest leaky BBBs and that the flow of EB or dextran may be unaffected in this condition. Leaky BBBs detected by EB or dextran were also largely in the somatosensory cortex (Figure 2, D, E, and H), but not hippocampus, suggesting an association of BBB deficit with the increase of BV density (Figure 2J). Also noteworthy is that the reduced DiI or blood flow was detected in the anesthetized mutant mice, implicating possible abnormal BV blockage/contraction induced by anesthesia.

Swollen astrocytes, disrupted vBMs, reduced pericytes, and impaired EC barrier in Neo$^{GFAP\text{-}CreER}$ *cortex.* To verify BBB leakage

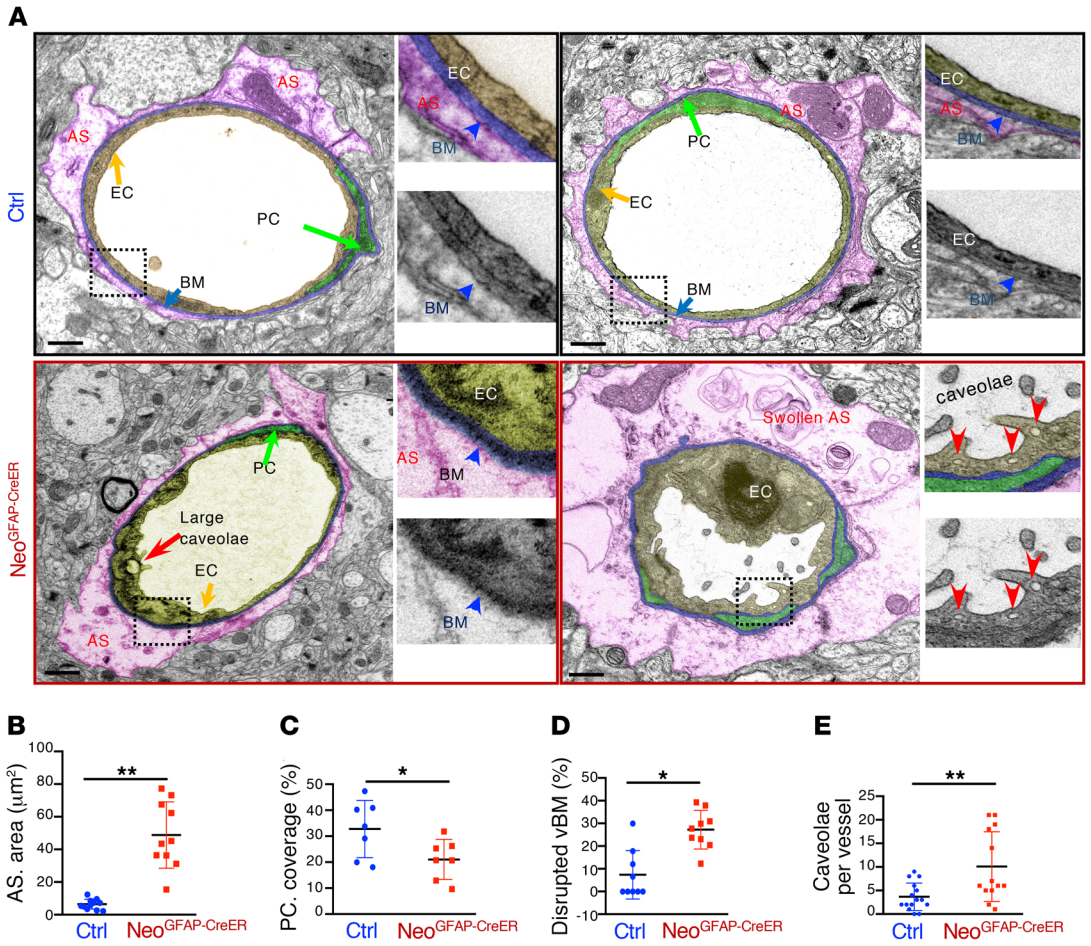

Figure 3. Swollen astrocytes, disrupted vBMs, reduced pericytes, and increased EC caveolae in *Neo*$^{GFAP\text{-}CreER}$ cortex by EM analysis. (**A**) Representative EM images of BVs in control (*Neo*$^{fl/fl}$) and *Neo*$^{GFAP\text{-}CreER}$ cortex (TAM at P30, EM at P60). Astrocytes are highlighted in pink, pericytes (PC) in light green, and EC in light yellow. Scale bars: 1 μm. (**B**) Quantification of astrocyte area. (**C**) Quantification of pericyte coverage of BVs. (**D**) Quantification of disrupted vBMs of BVs. (**E**) Quantification of EC caveolae per vessel. Data are represented as mean ± SEM (n = 7 to 13 vessels from 2 mice per group). *P < 0.05; **P < 0.01, Mann-Whitney U test.

in the mutant cortex, we examined BBB structure in control and *Neo*$^{GFAP\text{-}CreER}$ somatosensory cortices by electron microscopy (EM) analysis. Remarkably, perivascular astrocytes showed obviously enlarged cellular size in the *Neo*$^{GFAP\text{-}CreER}$ cortex, with an approximately 5-fold larger area than that of controls (Figure 3, A and B). The control vBM, a critical structure for BBB permeability (29), exhibited 3-layer high-density lines (Figure 3A). However, such high-density lines in the mutant vBMs were disrupted without a clear separation (Figure 3, A and D). The number of perivascular pericytes was reduced in the mutant vessels (Figure 3C). More caveolae-like vesicles were detected in the mutant ECs (Figure 3, A and E). These results demonstrate not only an astrocyte phenotype, but also multiple deficits in BV/BBBs, including disrupted vBMs, reduced pericytes, and impaired EC barrier.

We further confirmed the disrupted vBM and reduced pericytes by coimmunostaining analysis using antibodies against key components of vBM (e.g., laminin-γ1, laminin-α5, and collagen IV) and markers of pericytes (e.g., desmin and PDGFR-β) (30). As shown in Figure 4, A–F, laminin-γ1–, laminin-α5–, or collagen IV–labeled vBMs were evenly distributed along PECAM-1$^+$ vessels in control cortex, but in the mutant cortex, the vBMs marked by laminin-γ1, laminin-α5, or collagen IV were obviously abnormal (Figure 4, A, C, and E). They were absent in some areas, but formed aggregates at other areas of PECAM-1$^+$ vessels (Figure 4A). The pericytes marked by desmin or PDGFR-β were also markedly reduced in the mutant cortex as compared with those of controls (Figure 4, G–J). Further coimmunostaining with the apoptosis marker cleaved caspase-3 revealed that more pericytes underwent apoptosis in the Neo1 mutant cortex (Figure 4, K–L). These results, in line with the EM analysis, provide additional evidence for disrupted vBM and reduced pericytes in the astrocytic Neo1-KO cortex.

Finally, we examined EC tight junctions, caveolae, and fenestrae, critical structures for EC barrier function (31, 32), in control and Neo1 mutant cortex by coimmunostaining analyses. Few changes in zonula occludens-1 (ZO-1) and claudin-5, both markers of EC tight junctions, were detected in Neo1-KO cortical BVs (Supplemental Figure 3), suggesting tight junctions in the mutant ECs comparable to those of controls. However, both plasmalemma vesicle–associated protein (PLVAP), a marker

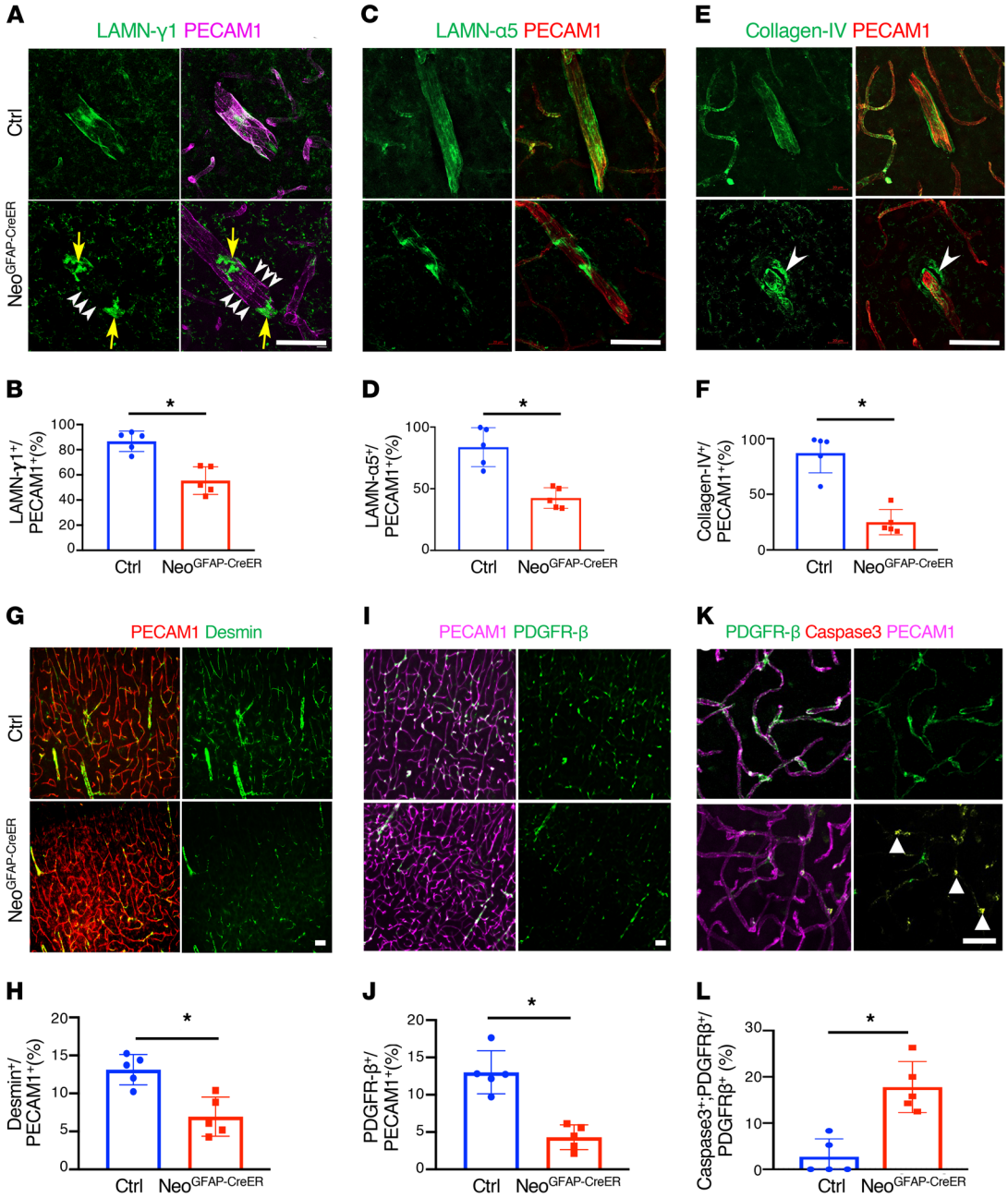

Figure 4. Disrupted vBMs and reduced pericytes in *Neo*$^{GFAP\text{-}CreER}$ cortex by coimmunostaining analysis. (**A**–**F**) Coimmunostaining analyses using indicated antibodies. Representative images of laminin-γ1 (**A**), laminin-α5 (**C**), and collagen IV (**E**) are shown. Quantification of laminin-γ1 (**B**), laminin-α5 (**D**), and collagen IV (**F**) in control (*Neo*$^{fl/fl}$) and *Neo*$^{GFAP\text{-}CreER}$ cortex are presented. In **A**, arrowheads indicate absent laminin-γ1 coverage and arrows indicate laminin-γ1 aggregates. In **E**, arrowheads show detached collagen IV from BVs. (**G**–**J**) Representative images of desmin (**G**) and PDGFR-β (**I**) marked pericytes, and quantification of desmin (**H**) and PDGFR-β (**J**) in control (*Neo*$^{fl/fl}$) and *Neo*$^{GFAP\text{-}CreER}$ cortex are shown. (**K** and **L**) Representative images (**K**) and quantification (**L**) of active caspase-3$^+$ pericytes in BVs of control and *Neo*$^{GFAP\text{-}CreER}$ cortex. Scale bars: 20 μm. Data are represented as mean ± SEM (n = 5 mice/group). *$P < 0.05$, Mann-Whitney U test.

of EC fenestrae, and caveolin-1, a marker of caveolae, were increased in the mutant ECs (Figure 5, A–D). These results, also in line with the EM studies, suggest an impairment in EC barrier function in the mutant BVs. Together, these results demonstrate decreases in vBMs and pericytes, but increases in EC caveolae and fenestrae in the Neo1 mutant cortex, which may underlie the increase of BBB permeability in the mutant cortex (Figure 5I).

Increased vein and capillaries and thinner arterioles in the Neo$^{GFAP\text{-}CreER}$ *cortex*. Both PLVAP and solute carrier family 16 member 1 (SLC16A) are selectively expressed in the ECs of venous capillaries, but not arterioles (33). We thus asked whether the increased BV density in the Neo1 mutant cortex is largely in the venous capillaries. To test this view, we carried out additional coimmunostaining analysis using antibodies against markers for arterioles, veins, and capillaries. As shown in Figure 5, F and H,

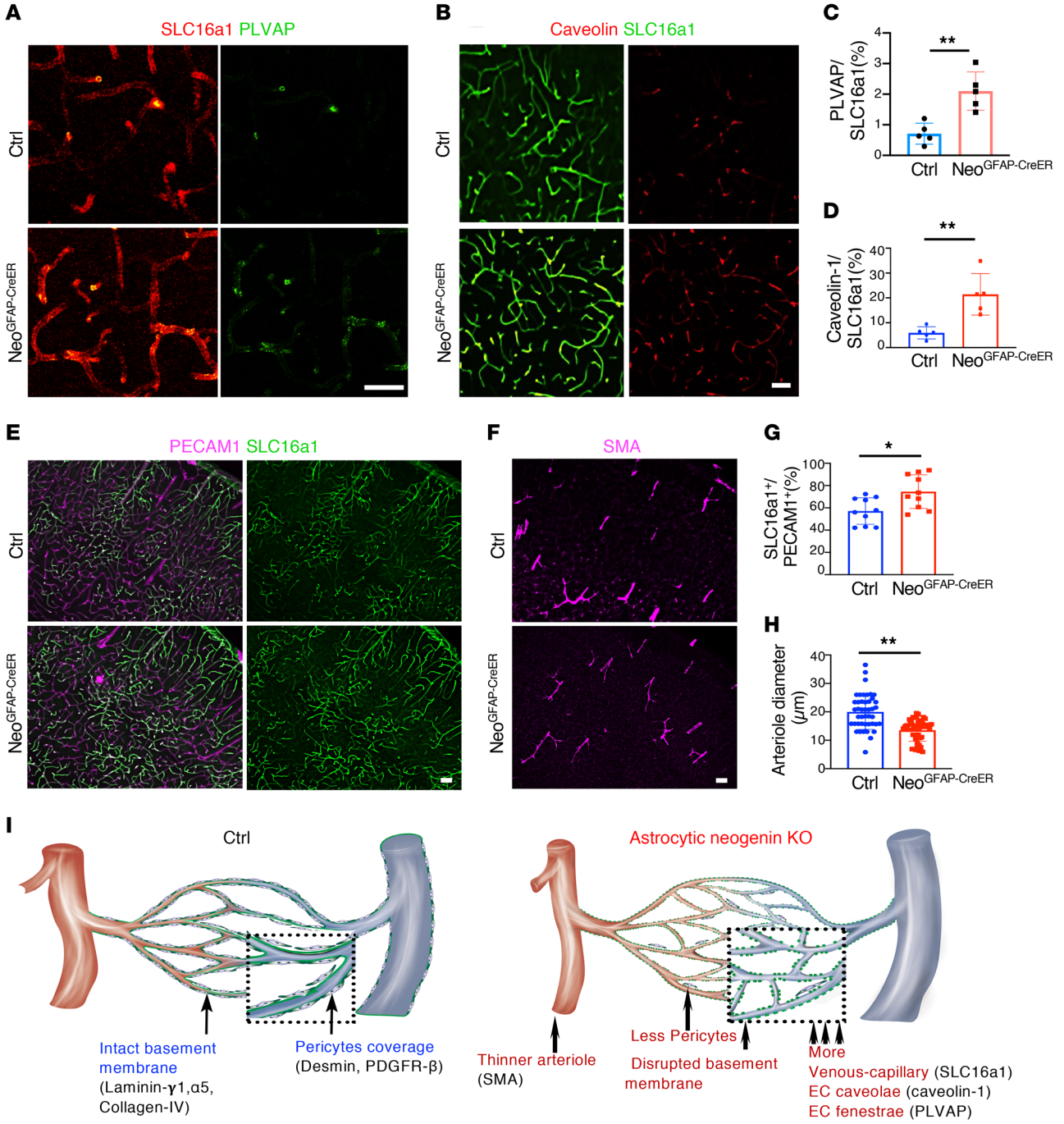

Figure 5. Impaired EC barrier, increased vein capillaries, and thinner arterioles in *Neo*$^{GFAP\text{-}CreER}$ cortex. (**A**, **B**, **E**, and **F**) Representative images of coimmunostaining analyses using indicated antibodies in control (*Neo*$^{fl/fl}$) and *Neo*$^{GFAP\text{-}CreER}$ cortex. (**C**, **D**, **G**, and **H**) Quantification analyses of data in **A**, **B**, **E**, and **F**. PLVAP is an EC fenestrae marker, caveolin-1 is a marker for caveolae, Slc16a1 is a venous-capillary marker, and labels arteriole. Scale bars: 20 μm. Data are represented as mean ± SEM (n = 5 mice/group). *P < 0.05; **P < 0.01, Mann-Whitney U test. (**I**) Schematic summary of vessel deficits in control and *Neo*$^{GFAP\text{-}CreER}$ cortex.

the arterioles labeled by anti–smooth muscle actin (anti-SMA) in the mutant cortex were obviously thinner in diameter than those of controls. However, more SLC16A1$^+$ ECs (vein and venous capillaries) were detected in the mutant cortex (Figure 5, E and G). Together, these results support the view that the increased vessel density and branch points in the Neo1 mutant cortex are likely to be veins and capillaries (Figure 5I).

To verify these BV changes detected by EM and coimmunostaining analyses, we examined protein levels of caveolin-1, PDGFRβ, CD146, EGFL7, SMA, and AQP4 by Western blot analysis. Indeed, increased caveolin-1, CD146, and EGFL7 levels, but decreased PDGFRβ and AQP4, were detected in the astrocytic Neo1-KO cortex (Supplemental Figure 4). These results, in line with the results by immunostaining analyses (Figure 4, I and J, and

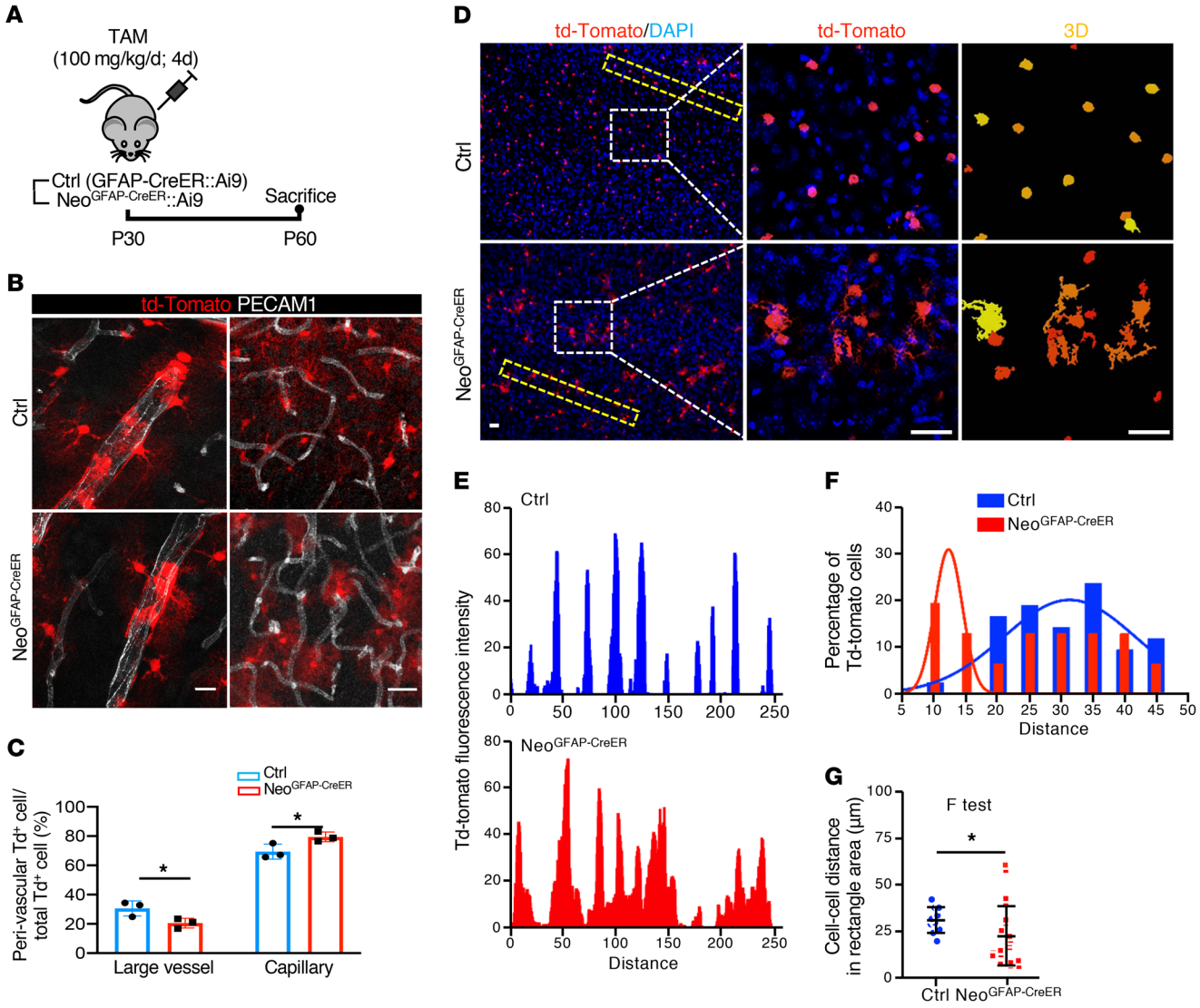

Figure 6. Altered astrocyte distribution in *Neo*$^{GFAP\text{-}CreER}$ cortex. (**A**) Schematic of the protocol performed in control (*GFAP-CreER;Ai9*) and *Neo*$^{GFAP\text{-}CreER}$*;Ai9* mice. (**B**) Representative images of td-Tomato$^+$ astrocytes and PECAM-1$^+$ BVs. (**C**) Quantification analysis of td-Tomato$^+$ astrocyte association with PECAM-1$^+$ (white) BVs in control and *Neo*$^{GFAP\text{-}CreER}$ cortex. (**D**) Representative images showing td-Tomato$^+$ astrocyte distribution. 3D reconstruction images are included in right panels. (**E**) Profile of rectangle area of td-Tomato$^+$ fluorescence in **D** analyzed by ZEN 2.3 lite. Cell-cell nuclear distance was quantified and is shown in **F** and **G**. (**F**) Histogram of average distance. Scale bars: 10 μm. Data are represented as mean ± SEM (n = 3 mice/group). *$P < 0.05$, Mann-Whitney U test (**C**); F test for variance analysis (**G**).

Figure 5, B and D), provide additional evidence for elevated damaged ECs, but reduced pericytes, in the Neo1 mutant cortex.

Altered astrocyte distribution in Neo$^{GFAP\text{-}CreER}$ *cortex.* To understand how astrocytic NEO1 regulates BV homeostasis and function, we determined whether astrocyte-BV interaction is impaired in Neo1 mutant mice. To this end, *Neo*$^{GFAP\text{-}CreER}$*;Ai9* mice were generated, as Ai9 expresses a Cre-dependent td-Tomato (34) that fluorescently labels astrocytes in control and Neo1 mutant mice. As shown in Figure 6, A and B, upon TAM injection at P30, control mice (*GFAP-CreER;Ai9*) at P60 showed evenly distributed td-Tomato$^+$ astrocytes in the cortex, while nearly all of their processes were in association with PECAM-1$^+$ BVs. In viewing td-Tomato$^+$ astrocyte association with PECAM-1$^+$ vessels in *Neo*$^{GFAP\text{-}CreER}$*;Ai9* mice, fewer td-Tomato$^+$ astrocytes were associated with large vessels, but more astrocytes were associated with small vessels (likely capillary) (Figure 6, B and C). The td-Tomato$^+$ astrocytes' distribution in the mutant cortex was obviously uneven (Figure 6D). Many clusters of td-Tomato$^+$ astrocytes were observed in the mutant cortex (Figure 6D). These results implicate a deficit in astrocyte distribution, a prominent feature of astrocytes with nonoverlapping territories (35). To further test this view, we examined td-Tomato$^+$ astrocyte distribution by measuring their cell-to-cell distance. As shown in Figure 6, E–G, td-Tomato$^+$ astrocytes in the control cortex were evenly distributed without overlapping territories and most td-Tomato$^+$ astrocytes had a cell-to-cell distance of 30–35 μm. In contrast, many td-Tomato$^+$ astrocytes in the mutant cortex were distributed as clusters in some areas, but absent in other areas, displaying variable cell-to-cell distances (Figure 6, D–G). Many mutant astrocytes (~20%) were closely distributed within 5–10 μm of cell-to-cell distance (Figure 6, F and G). 3D reconstruc-

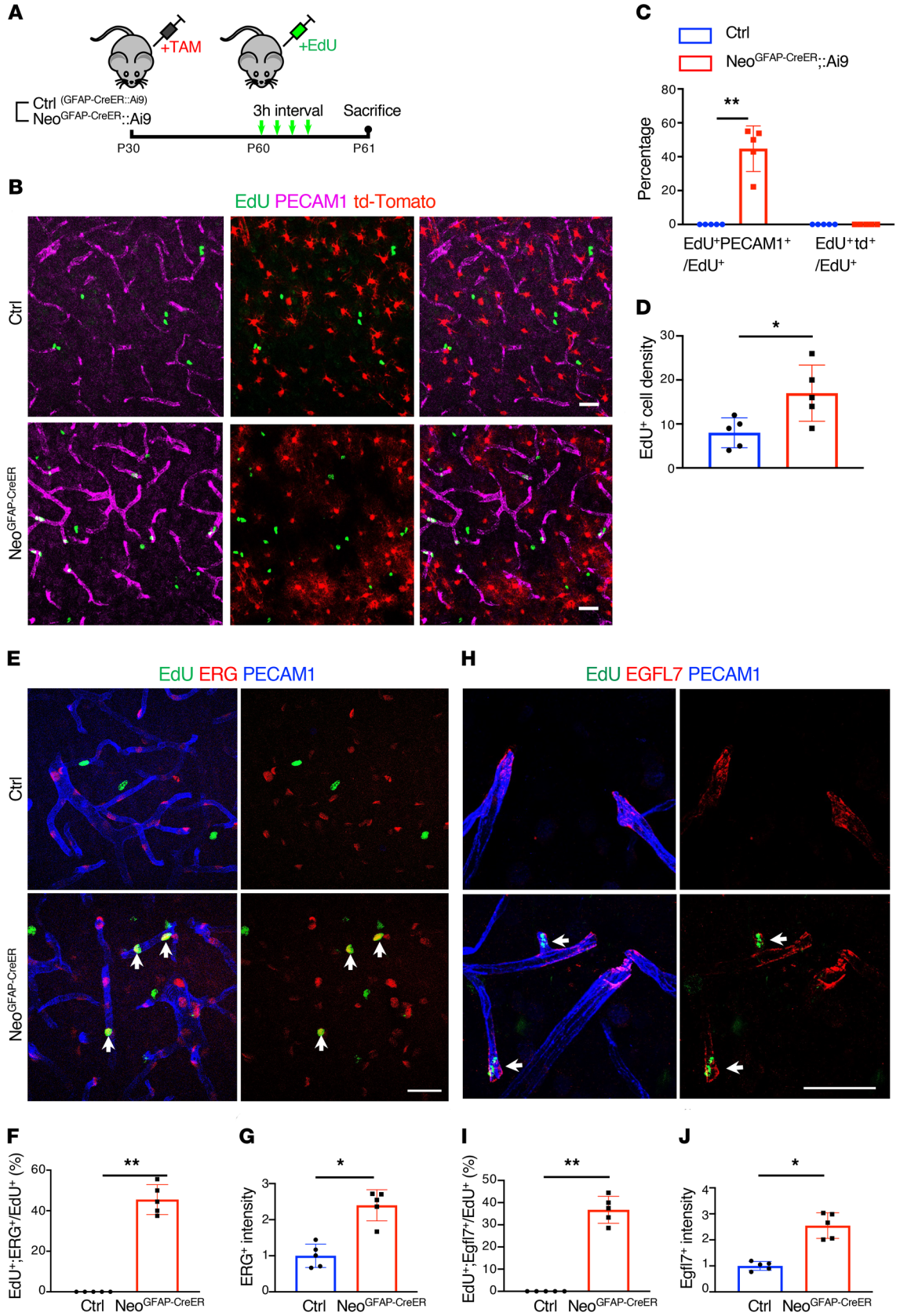

Figure 7. Elevated tip EC proliferation in *Neo*$^{GFAP\text{-}CreER}$ cortex. (**A**) Schematic of TAM and EdU injection protocol in control (*GFAP-CreER;Ai9*) and *Neo*$^{GFAP\text{-}CreER}$*;Ai9* mice. (**B**) Representative images of cortical brain sections coimmunostained with EdU (green), PECAM-1 (magenta), and td-Tomato (red). (**C** and **D**) Quantification analyses of data in **B**. (**E** and **H**) Representative images of cortical brain sections coimmunostained with indicated antibodies. (**F**–**J**) Quantitative analyses of data in **E** and **H**, respectively. Scale bars: 20 μm. Data in **C**, **D**, **F**, **G**, **I**, and **J** are represented as mean ± SEM (n = 5 mice/group). *$P < 0.05$; **$P < 0.01$, Mann-Whitney U test

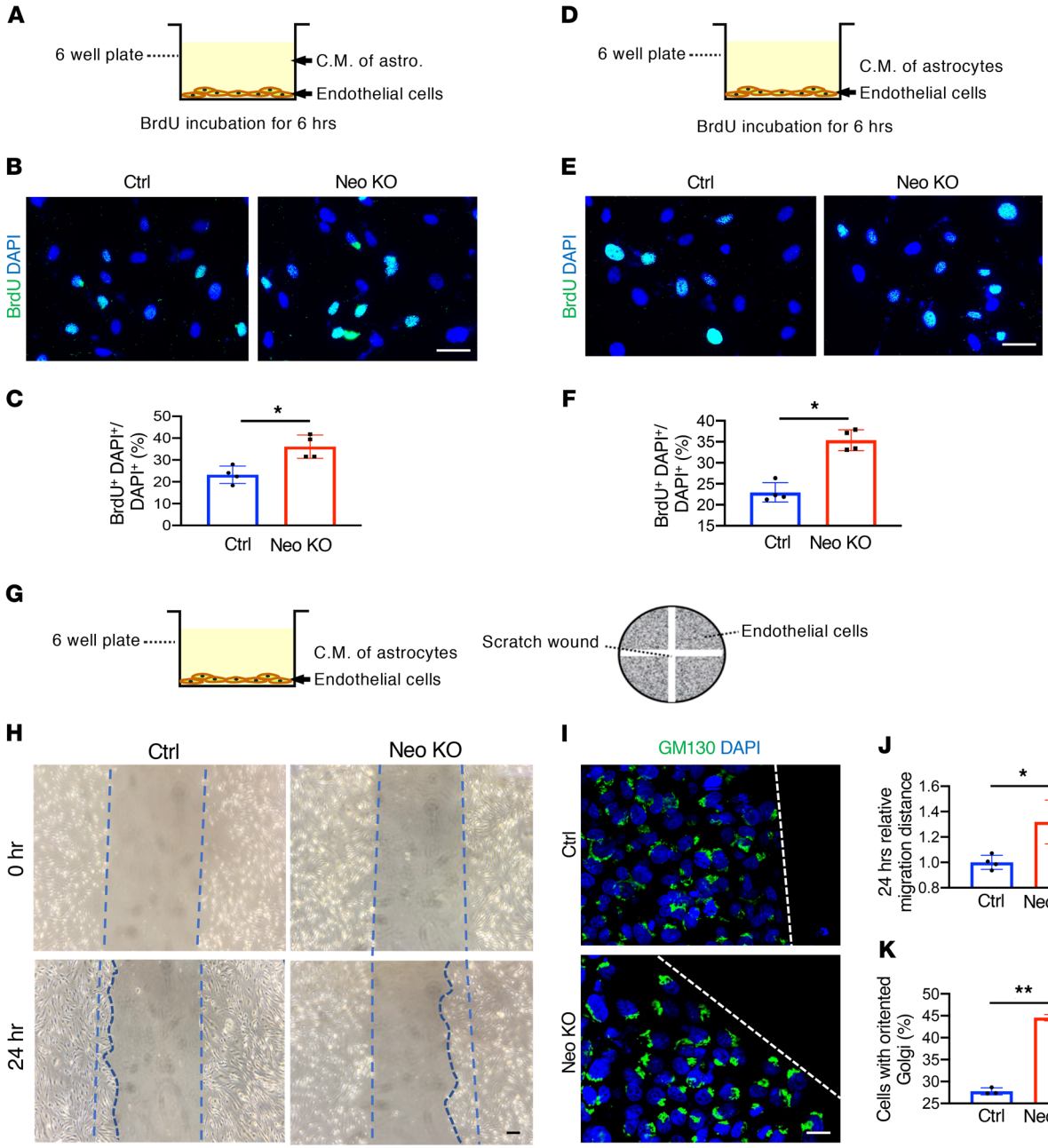

Figure 8. Increased EC proliferation and migration in HUVEC cultures exposed to Neo1-KO astrocytes or their CM. (**A**–**C**) Increased EC proliferation in HUVECs cocultured with Neo1-KO astrocytes. (**A**) Schematic of coculture of HUVECs with cortical astrocytes of control and Neo-KO. BrdU was incubated for 4 hours. (**B**) Representative images of BrdU$^+$ HUVECs. (**C**) Quantitative analysis of data in **B**. Data are represented as mean ± SEM (n = 4 experiments of astrocytes from *Neo*$^{GFAP\text{-}CreER}$ with 4-OH-TAM). (**D**–**F**) Increased EC proliferation in HUVECs exposed to CM of Neo1-KO astrocytes. (**D**) Schematic of the culture. BrdU was incubated for 6 hours. (**E**) Representative images of BrdU$^+$ HUVECs. (**F**) Quantification analysis of data in **E**. Data are represented as mean ± SEM (n = 4 experiments with astrocytes from *Neo*$^{GFAP\text{-}CreER}$ [+TAM] and its control group). (**G**–**K**) Increased EC migration in HUVECs exposed to CM of Neo1-KO astrocytes. (**G**) Schematic of HUVEC migration assay. The HUVECs were cultured with CM of astrocytes in a 6-well plate (left panel), and were scratched for the wound-healing migration assay (right panel). (**H**) Representative images of HUVEC migration 24 hours after wound scratching. (**I**) Representative images of HUVECs that were cultured with CM of astrocytes and immunostained with indicated antibodies. (**J**) Quantification analyses of data in **H**. Data are represented as mean ± SEM (n = 4 experiments from *Neo*$^{GFAP\text{-}CreER}$ and its control group astrocytes). (**K**) Quantification of data in **I**. Data are represented as mean ± SEM (n = 3 experiments from *Neo*$^{GFAP\text{-}CreER}$ and its control group astrocytes). Scale bars: 20 μm. $^*P < 0.05$; $^{**}P < 0.01$, Mann-Whitney U test.

tion of these astrocytes provided additional support for their overlapping territories in the mutant cortex (Figure 6D). These results demonstrate the necessity of astrocytic NEO1 in maintaining an astrocyte distribution pattern. These mutant clustered astrocytes were not reactive, as little to no GFAP (a marker for reactive astrocytes in cortex) was detected in the mutant td-Tomato$^+$ astrocytes (Supplemental Figure 6).

Elevations in tip EC proliferation in Neo$^{GFAP\text{-}CreER}$ *cortex.* We then asked whether the clustered td-Tomato$^+$ astrocytes resulted from an alteration in astrocytic proliferation. Mice (*GFAP-CreER;Ai9*

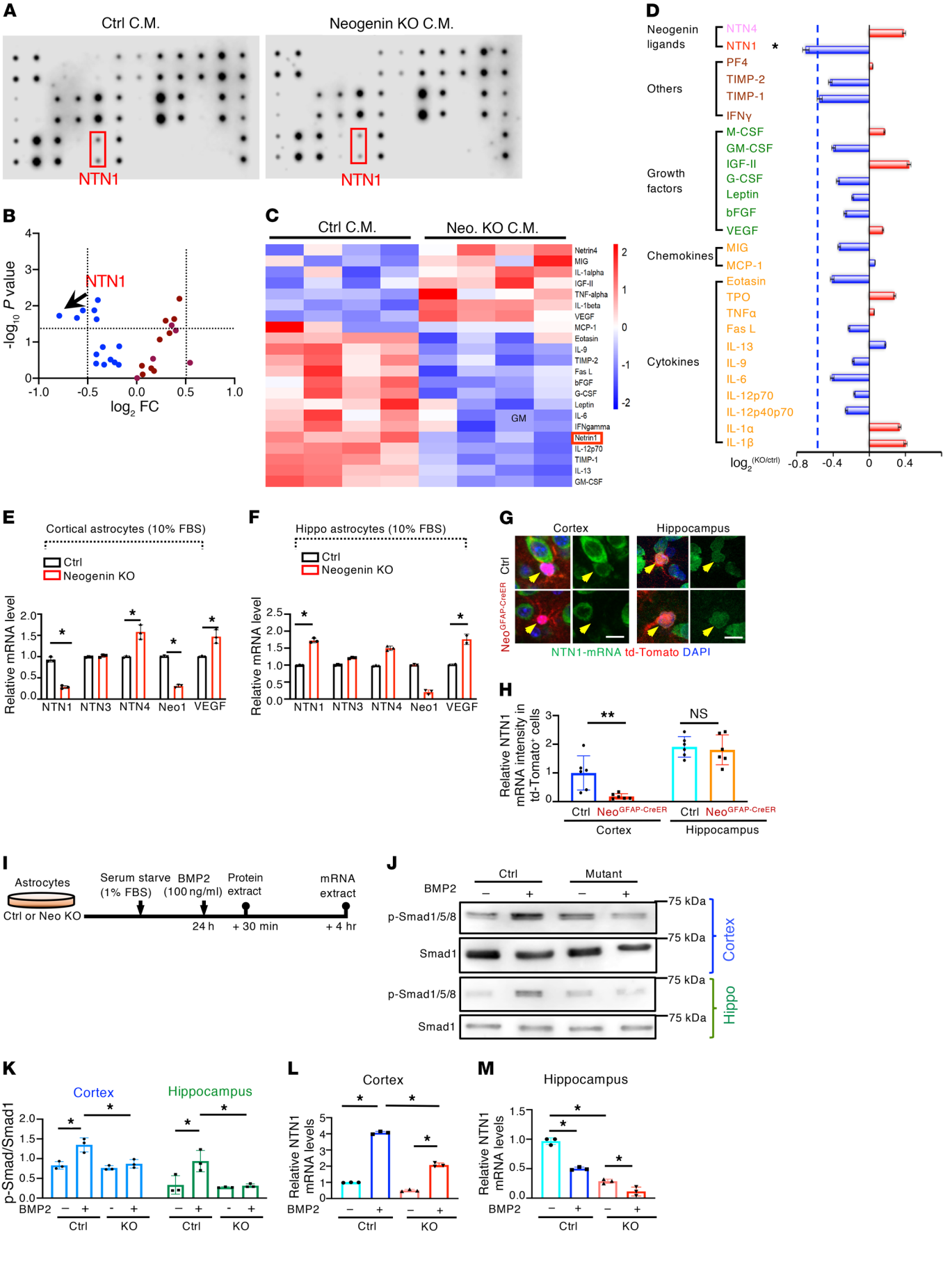
A
Ctrl C.M.
Neogenin KO C.M.
NTN1
NTN1
B
-log10 P value
log2 FC
NTN1
C
Ctrl C.M.
Neo. KO C.M.
Netrin4
MIG
IL-1alpha
IGF-II
TNF-alpha
IL-1beta
VEGF
MCP-1
Eotasin
IL-9
TIMP-2
Fas L
bFGF
G-CSF
Leptin
IL-6
IFNgamma
Netrin1
IL-12p70
TIMP-1
IL-13
GM-CSF
GM
D
Neogenin ligands
NTN4
NTN1
Others
PF4
TIMP-2
TIMP-1
IFNγ
Growth factors
M-CSF
GM-CSF
IGF-II
G-CSF
Leptin
bFGF
VEGF
Chemokines
MIG
MCP-1
Cytokines
Eotasin
TPO
TNFα
Fas L
IL-13
IL-9
IL-6
IL-12p70
IL-12p40p70
IL-1α
IL-1β
log2(KO/ctrl)
E
Cortical astrocytes (10% FBS)
Ctrl
Neogenin KO
Relative mRNA level
NTN1 NTN3 NTN4 Neo1 VEGF
F
Hippo astrocytes (10% FBS)
Ctrl
Neogenin KO
Relative mRNA level
NTN1 NTN3 NTN4 Neo1 VEGF
G
Cortex
Hippocampus
Ctrl
NeoGFAP-CreER
NTN1-mRNA td-Tomato DAPI
H
Relative NTN1 mRNA intensity in td-Tomato+ cells
**
NS
Ctrl NeoGFAP-CreER Ctrl NeoGFAP-CreER
Cortex
Hippocampus
I
Astrocytes
Ctrl or Neo KO
Serum starve (1% FBS)
BMP2 (100 ng/ml)
Protein extract
mRNA extract
24 h
+ 30 min
+ 4 hr
J
Ctrl
Mutant
BMP2
p-Smad1/5/8
Smad1
p-Smad1/5/8
Smad1
75 kDa
Cortex
Hippo
K
Cortex
Hippocampus
p-Smad/Smad1
BMP2
Ctrl KO Ctrl KO
L
Cortex
Relative NTN1 mRNA levels
BMP2
Ctrl KO
M
Hippocampus
Relative NTN1 mRNA levels
BMP2
Ctrl KO

Figure 9. Reduced NTN1 in Neo1-KO cortical astrocytes. (**A**–**D**) Antibody array analysis. The nitrocellulose membranes containing 26 antibodies (see Supplemental Figure 10A) were first incubated with biotin-conjugated proteins from CM of control and Neo1-KO astrocytes, respectively, washed, and then incubated with HRP-streptavidin, according to the manufacturer's instructions. (**A**) Representative images of the antibody array blots. NTN1 is highlighted in red. (**B**) Volcano plot analysis showing reduced NTN1 in the CM of Neo1-KO astrocytes. (**C**) Heatmap analysis (n = 4). (**D**) Quantification analysis. Data are represented as mean ± SEM (n = 4). (**E** and **F**) Quantitative PCR (qPCR) analysis of indicated gene expression in cortical (**E**) and hippocampal astrocytes (**F**) (cultured in the presence of 10% FBS). Values were normalized to GAPDH levels and controls. Data are represented as mean ± SEM (n = 3 experiments /group). (**G** and **H**) FISH analysis of NTN1 mRNAs in td-Tomato$^+$ astrocytes in control (*GFAP-CreER;Ai9*) and *Neo$^{GFAP\text{-}CreER}$;Ai9* cortex and hippocampus. (**G**) Representative images. Scale bar: 5 μm. (**H**) Quantification analysis of data in **G**. Data are represented as mean ± SEM (n = 6 slides/group). (**I**–**M**) BMP2 induction of phospho-Smad$_{1/5/8}$ and NTN1 expression in cortical and hippocampal astrocytes (cultured in the presence of 1% FBS) from control and Neo1-KO mice. (**I**) Illustration of protocol of BMP2 treatment.(**J**) Western blot analyses using indicated antibodies. (**K**) Quantification of data in **J**. (**L** and **M**) qPCR analyses of BMP2-induced NTN1 mRNAs in cortical (**L**) and hippocampal (**M**) astrocytes. Data are represented as mean ± SEM (n = 3 experiments). *P < 0.05; **P < 0.01, 2-way ANOVA.

and *Neo$^{GFAP\text{-}CreER}$;Ai9*) were injected with 5-ethynyl-2′-deoxyuridine (EdU) (a marker of cell proliferation) 24 hours before sacrifice (Figure 7A). Immunostaining analysis showed little to no EdU$^+$ signal in td-Tomato$^+$ astrocytes in both control and mutant cortices (Figure 7, B and C), eliminating the possibility of astrocyte proliferation as causing their clustered distribution. Interestingly, EdU$^+$ cell density was higher in the mutant cortex than in that of controls (Figure 7D) and many EdU$^+$ cells had a close association with PECAM-1$^+$ ECs in the mutant cortex (Figure 7, B and C), implicating an increase in EC proliferation. We thus further tested this view by coimmunostaining analysis of EdU with PECAM-1 and ETS-related gene (ERG), an EC-specific transcriptional factor (36). Indeed, more EdU$^+$ERG$^+$ signals were detected in *Neo$^{GFAP\text{-}CreER}$* cortical BVs (Figure 7, E–G), supporting the view that there was increased EC proliferation in the mutant cortex. We then determined whether the increased proliferative ECs were tip ECs by coimmunostaining analysis of EdU with PECAM-1 and epidermal growth factor–like domain 7 (EGFL7), a protein highly expressed in proliferative tip ECs. More EGFL7$^+$ signals were detected in PECAM-1$^+$ ECs (Figure 7, H and J), and many (~36.8%) of the EGFL7$^+$ tip cells were EdU$^+$ (Figure 7, H–J), demonstrating increased proliferative tip ECs in the mutant cortex. This view was further supported by the observation of increased VGLUT1 (another marker of tip cell) in PECAM-1$^+$ BVs in the mutant cortex (Supplemental Figure 5).

Elevation of EC proliferation and migration in EC cultures exposed to the conditioned medium of Neo1-KO astrocytes. To understand how NEO1 deficiency in astrocytes results in increased EC proliferation, we carried out coculture assays. Human umbilical veins ECs (HUVECs) or mouse brain microvascular ECs (MBMEC) were cocultured with primary astrocytes from neonatal control or Neo1-KO (*Neo$^{GFAP\text{-}Cre}$* or *Neo$^{GFAP\text{-}CreER}$*) mice in a Transwell assay, as illustrated in Figure 8, Supplemental Figure 7, and Supplemental Figure 9. BrdU (3 μg/mL) was added into the medium 4 hours before termination of the culture (Figure 8A). As shown in Figure 8, B and C, BrdU$^+$ EC density was higher upon coculturing with Neo1-KO astrocytes, as compared with those ECs cocultured with control astrocytes, indicating an increase in EC proliferation by Neo1-KO astrocytes. Because these astrocytes did not directly contact ECs in the Transwell coculture assay, the increased EC proliferation is likely due to secreted factors from Neo1-KO astrocytes. To test this view, we cultured HUVECs or MBMECs in the presence of conditioned medium (CM) from control or Neo1-KO astrocytes. EC proliferation (visualized by BrdU$^+$ cells) was higher in the presence of CM of Neo1-KO astrocytes than in that of control CM (Figure 8, D–F; and Supplemental Figure 9), supporting this view.

In addition to EC proliferation, we examined EC migration, another event critical for angiogenesis (37), by wound-healing assay, as illustrated in Figure 8G. HUVECs were cultured with the CM of Neo1-KO astrocytes, and EC migratory distance following the scratch was measured. As shown in Figure 8, H and J, much faster migration in ECs cultured with the CM of Neo1-KO astrocytes was detected. In addition, the percentage of ECs with GM130$^+$ Golgi apparatus facing the migratory direction (38) was higher in ECs cultured with the CM of Neo1-KO astrocytes (Figure 8, I and K), supporting increased EC migration. This view was further supported by an EC Transwell migration assay (Supplemental Figure 9, G–I). Notice that no cleaved caspase-3$^+$ signal was detected of the ECs (Supplemental Figure 9F), suggesting little to no apoptosis occurred in these ECs cultured with astrocyte CM. Together, these results suggest that the CM of Neo1-KO astrocytes contains a protein or proteins that regulate EC proliferation and/or migration.

Reduced NTN1 in NEO1-KO cortical astrocytes. We next screened for potential protein or proteins in the CM of astrocytes that may regulate EC proliferation by use of an antibody array assay. As illustrated in Figure 9A and Supplemental Figure 10A, nitrocellulose membranes containing various antibodies against proteins implicated in angiogenesis (see Supplemental Figure 10A), which include VEGF1, M/G-CSF, IGF-1I, bFGF, TIMP1, chemokines, cytokines, and NTN1 and NTN4, ligands of NEO1, were incubated with biotinylated protein samples from CM of control or Neo1-KO astrocytes, respectively. The positive signals were detected by streptavidin after washes. Interestingly, NTN1, but not NTN4, was lower in the CM of Neo1-KO astrocytes than that of control astrocytes (Figure 9, B–D). In addition, TIMP-1, an inhibitor of metalloproteinases (MMPs) critical for cell adhesion and migration and angiogenesis (39) was also decreased in the CM of mutant astrocytes (Figure 9, B–D).

We further addressed how Neo1-KO astrocytes had reduced NTN1, but not NTN4, levels in their CM. To this end, mRNA levels of NTN family members, including NTN1, -3, and -4, as well as VEGF-a were examined in control and Neo1-KO cortical and hippocampal astrocytes (cultured in the presence of 10% FBS) by real-time PCR analysis. Remarkably, NTN1 was selectively reduced in cortical, but not hippocampal, Neo1-KO astrocytes, while NTN4 was increased in both cortical and hippocampal Neo1-KO astrocytes (Figure 9, E and F). The VEGF-a mRNA levels were also increased in both cortical and hippocampal Neo1-KO astrocytes (Figure 9, E and F). In line with this view were observations of reduced NTN1, but increased VEGF, transcripts in the *neo$^{GFAP\text{-}CreER}$* cortex (Supplemental Figure 10, B–D).

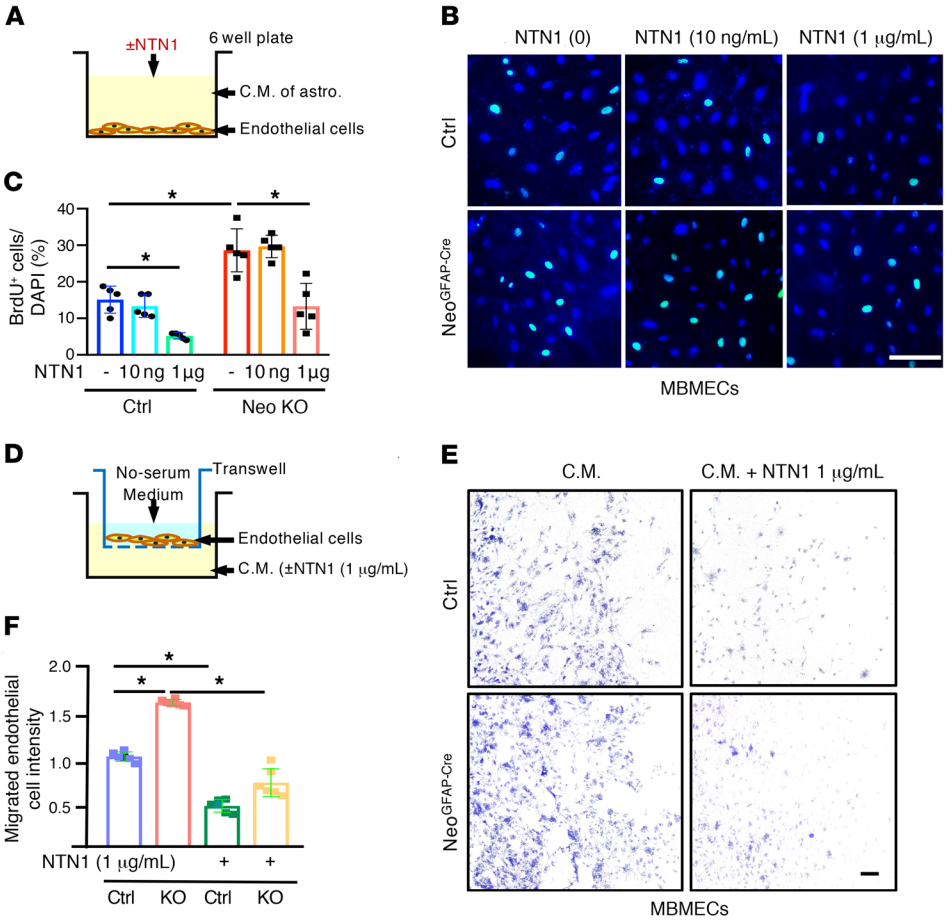

Figure 10. NTN1 inhibition of EC proliferation and migration induced by CM of Neo1-KO astrocytes. (**A**–**C**) NTN1 (1 μg/mL) inhibition of MBMEC proliferation. (**A**) Schematic of NTN1 administration in MBMEC cultures in the presence of CM of astrocytes. BrdU (3 μg/mL) was incubated for 6 hours. (**B**) Representative images of BrdU+ MBMECs. (**C**) Quantification analysis of data in **B**. (**D**–**F**) NTN1 inhibition of MBMEC migration. (**D**) Schematic of NTN1 administration in a Transwell assay to access MBMEC migration. (**E**) Representative images of MBMECs (stained with crystal violet). (**F**) Quantification analysis of data in **E**. Data are represented as mean ± SEM (n = 5–6 coverslips /group). *P < 0.05, 2-way ANOVA. Scale bars: 20 μm.

NTN1 is believed to be expressed mainly in pericytes in adult mouse brain, based on findings in the single-cell RNA-Seq database (http://betsholtzlab.org/VascularSingleCells/database.html.). However, based on the Allen Brain Atlas In Situ Hibridization database, NTN1 appears to be expressed in a subset of neurons. Our results suggest that NTN1 was expressed in astrocytes that were selectively reduced in Neo1-KO cortical astrocytes. To address this issue, we further examined NTN1 expression in *GFAP-CreER;Ai9* (control) and *Neo*$^{GFAP\text{-}CreER}$*;Ai9* brain sections by FISH. NTN1 transcripts were detected by antisense, but not sense, probes (Supplemental Figure 8), suggesting NTN1 probe specificity. Interestingly, these NTN1-positive signals were detected in a subset of neurons and td-Tomato+ astrocytes in control brains (Figure 9, G and H). However, NTN1 signals were remarkably reduced in NEO1-KO astrocytes, but not neurons, in the cortex, but not hippocampus (Figure 9, G and H). These results, in line with the reverse transcriptase PCR (RT-PCR) results (Figure 9, E and F), provide additional evidence for cortical astrocytic NTN1 expression that is upregulated by astrocytic NEO1. This view was further verified by RNA-scope analysis, a high resolution in situ method (Supplemental Figure 8, B and C).

In addition to NTNs, NEO1 is a coreceptor for BMPs involved in multiple BMP-regulated cellular processes, including cortical astrogliogenesis (40). We thus asked whether BMP regulates NTN1 expression in astrocytes in a NEO1-dependent manner. To this end, we examined BMP2-induced phospho-Smad$_{1/5/8}$ signaling (30 minutes after BMP2 stimulation, by Western blot) and NTN1 expression (4 hours after BMP2 stimulation, by RT-PCR) in both cortical and hippocampal astrocytes that were cultured under serum-starved condition (1% FBS) for 24 hours to allow efficient BMP2 stimulation (Figure 9, I–M). Upon BMP2 stimulation (for 30 minutes), phospho-Smad$_{1/5/8}$ was induced in both cortical and hippocampal astrocytes, which were impaired in Neo1-KO astrocytes (Figure 9, I–K). However, BMP2 increased NTN1's expression only in control cortical, but not hippocampal, astrocytes; this was abolished in Neo1-KO cortical astrocytes (Figure 9, I, L, and M). These results thus support the view for brain region–selective regulation of astrocytic NTN1 expression by BMP2/NEO1 signaling.

NTN1 inhibition of EC proliferation and migration in a dose-dependent manner. We then determined whether reduced NTN1 is responsible for EC proliferation and migration phenotypes induced by Neo1-KO astrocytes. To this end, we first examined NTN1's effect on EC proliferation and migration by the EC-astrocyte coculture Transwell assay, as illustrated in Figure 10A. In light of a previous report that NTN1 regulates EC proliferation in a dose-dependent manner (41), both low (10 ng/mL) and high (1 μg/mL) concentrations of NTN1 were added to the medium of the coculture assay. The 10 ng/mL NTN1 showed an increased EC proliferation in MBMEC cultures (with M200 culture medium) (Supplemental Figure 11), in line with a previous report (41). However, NTN1 at a concentration of 1 μg/mL reduced BrdU+ MBMECs cocultured with the CM of control or Neo1-KO astro-

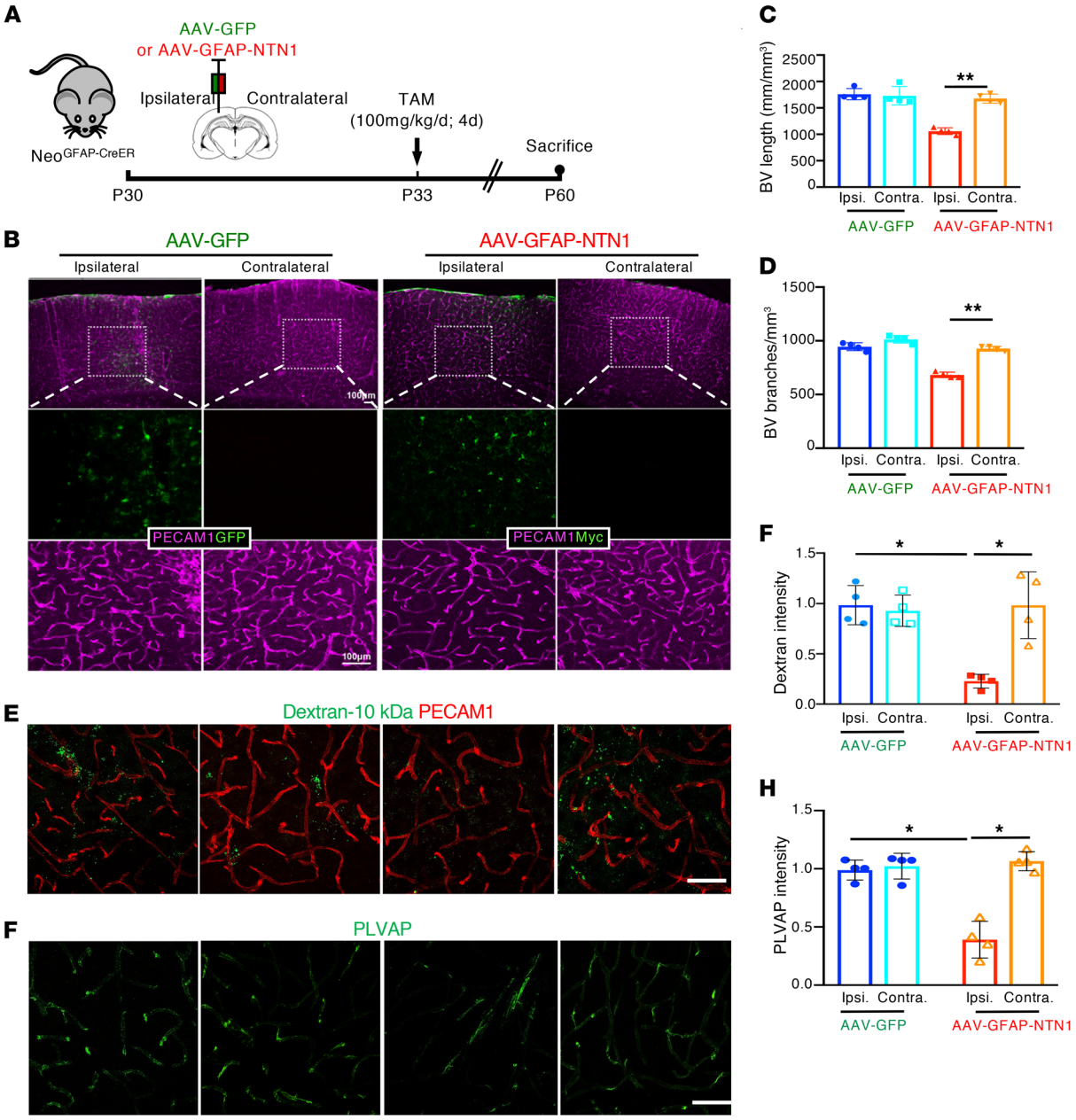

Figure 11. NTN1 amelioration of phenotypes of BV increase and BBB leakage in Neo1-KO cortex. (**A**) Schematic of protocol of AAV-GFP and AAV-GFAP-NTN1 viruses and TAM injections. AAV-GFAP-NTN1 encoding NTN1 fusion protein (NTN1-myc-his-P2A-mCherry) under control of GFAP promoter was injected into left side of *Neo*$^{GFAP\text{-}CreER}$ cortex (ipsilateral side) at P30. (**B**) Representative images of immunostaining using indicated antibodies. P60 *Neo*$^{GFAP\text{-}CreER}$ cortices were injected with AAV-GFP or AAV-GFAP-NTN1, respectively. Scale bars: 100 μm. (**C** and **D**) Quantitative analyses of BV length (**C**) and branches (**D**). (**E**) Representative images showing 10 kDa dextran leakage in ipsilateral and contralateral cortices injected with AAV-GFP or AAV-GFAP-NTN1, respectively. (**F**) Quantitative analyses of data in **E**. (**G**) Representative images showing PLVAP staining in ipsilateral and contralateral cortices injected with AAV-GFP or AAV-GFAP-NTN1, respectively. (**H**) Quantitative analyses of data **G**. Data are represented as mean ± SEM (n = 4 mice/group). *P < 0.05; **P < 0.01, 2-way ANOVA. Scale bars: 20 μm.

cytes (Figure 10, A–C). In addition, NTN1 (1 μg/mL) decreased EC migration induced by Neo1-KO astrocytes (Figure 10, D–F). These NTN1 effects were verified in HUVEC-astrocyte cocultures (Supplemental Figure 12) and suggest that a high concentration of NTN1 is sufficient to suppress EC proliferation and migration.

NTN1 amelioration of the deficit in BV/BBB and the alteration in astrocyte distribution in Neo$^{GFAP\text{-}CreER}$ *cortex.* To investigate whether astrocytic NTN1 expression could restore BV/BBB deficits in Neo1 mutant mice, AAV-GFAP-NTN1 virus, which encodes chicken NTN1-Myc-His-2A-mCherry under the control of the GFAP promoter, was generated (see Supplemental Figure 13). This AAV-GFAP-NTN1 and its control virus (AAV-GFAP-GFP) were injected into the left side of the *Neo*$^{GFAP\text{-}CreER}$ cortex at P30. Mice were treated with TAM (i.p., 100 mg/kg/d, once per day for 4 days) at P33 and sacrificed at P60 (Figure 11A). Brain sections were subjected to immunostaining analysis using indicated antibodies. As shown

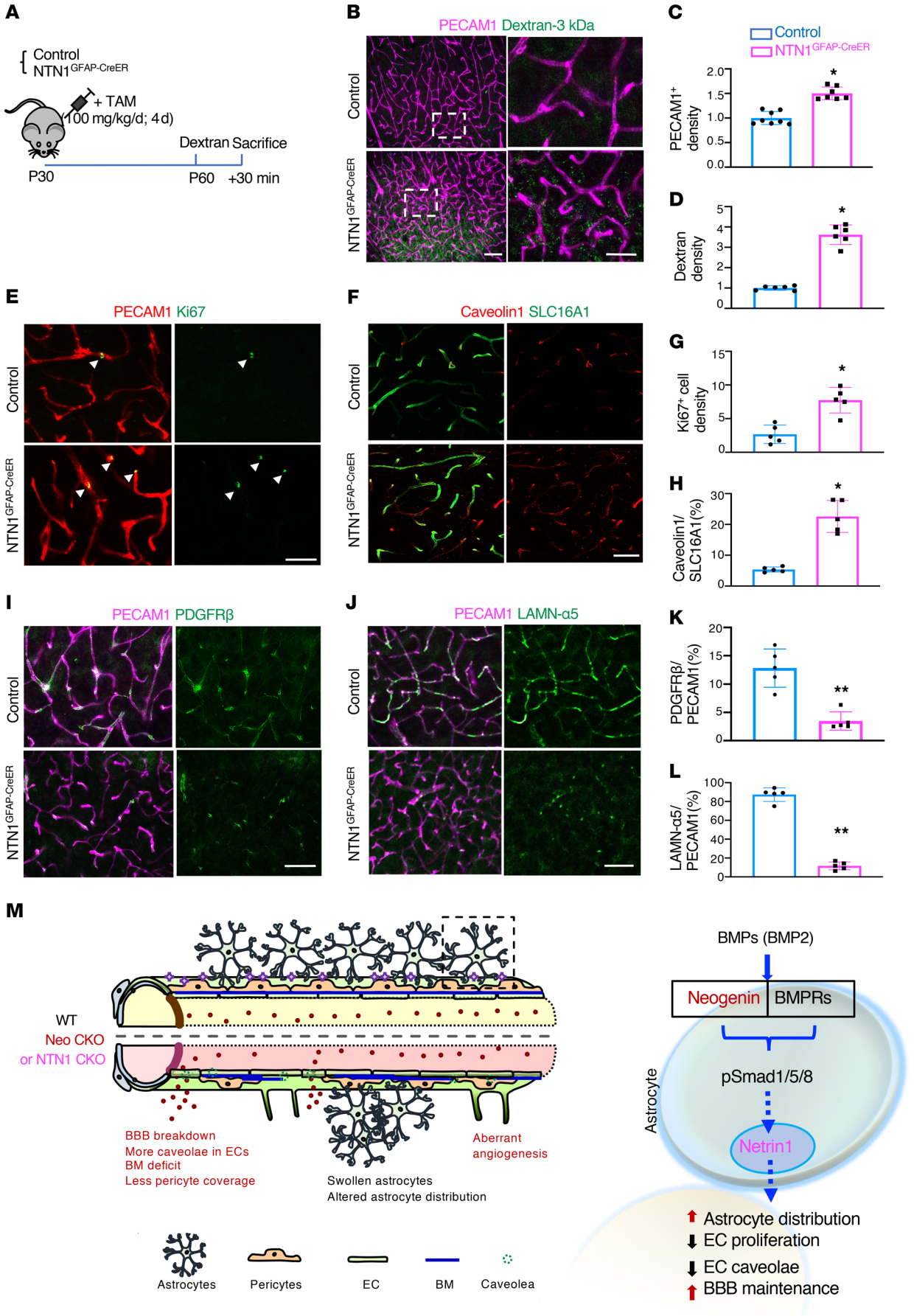
A
Control
NTN1GFAP-CreER
+ TAM
100 mg/kg/d; 4 d)
Dextran Sacrifice
P30
P60 +30 min
B
PECAM1 Dextran-3 kDa
Control
NTN1GFAP-CreER
C
Control
NTN1GFAP-CreER
PECAM1+ density
D
Dextran density
E
PECAM1 Ki67
F
Caveolin1 SLC16A1
G
Ki67+ cell density
H
Caveolin1/ SLC16A1(%)
I
PECAM1 PDGFRβ
J
PECAM1 LAMN-α5
K
PDGFRβ/ PECAM1(%)
L
LAMN-α5/ PECAM1(%)
M
WT
Neo CKO
or NTN1 CKO
BBB breakdown
More caveolae in ECs
BM deficit
Less pericyte coverage
Swollen astrocytes
Altered astrocyte distribution
Aberrant angiogenesis
Astrocytes
Pericytes
EC
BM
Caveolea
BMPs (BMP2)
Neogenin
BMPRs
pSmad1/5/8
Netrin1
Astrocyte
Astrocyte distribution
EC proliferation
EC caveolae
BBB maintenance

Figure 12. Increased BV density, leaky BBB, and fewer pericytes and vBMs in astrocytic Ntn1-KO cortex. (**A**) Schematic of experiments. *NTN1*$^{GFAP\text{-}CreER}$ and littermate control (*NTN1*$^{fl/fl}$) mice (at P30) were injected with TAM, and mice at P60 were anesthetized, tail injected with 3 kDa dextran, and sacrificed 30 minutes after dextran injection. (**B**) Representative images of BVs (magenta) and dextrans (green) in cortices of control and *NTN1*$^{GFAP\text{-}CreER}$ mice. (**C** and **D**) Quantitative analyses of PECAM-1$^+$ BV density (**C**) and dextron$^+$ intensity (**D**). (**E** and **G**) Representative images (**E**) and quantification analysis (**G**) of BV-EC proliferation in the cortices of control and *NTN1*$^{GFAP\text{-}CreER}$ mice. Arrowheads indicate Ki67$^+$ cells. (**F** and **H**) Representative images (**F**) and quantification analysis (**H**) of caveolin1$^+$ capillary-venous in cortices of control and *NTN1*$^{GFAP\text{-}CreER}$ mice. (**I** and **K**) Representative images (**I**) and quantification (**K**) of PDGFRβ$^+$ pericytes in cortexes of control and *NTN1*$^{GFAP\text{-}CreER}$ mice. (**J** and **L**) Representative images (**J**) and quantification (**L**) of laminin-α5$^+$ BVs in cortices of control and *NTN1*$^{GFAP\text{-}CreER}$ mice. (**M**) Summary of phenotypes and illustration of a working model for astrocytic Neo1 to regulate BV hemostasis through NTN1. Scale bars: 20 μm. Data are represented as mean ± SEM (n = 5 mice). *P < 0.05; **P < 0.01 Mann-Whitney U test.

in Figure 11, B–D, GFP fluorescence (for AAV-GFAP-GFP) and Myc$^+$ fluorescence (for AAV-GFAP-NTN1) were detected on the injection side, but not contralateral side, of the mutant cortex (Figure 11B), demonstrating their expression in astrocytes. Western blot analysis verified AAV-GFAP-NTN1 expression at a concentration of approximately 1.56 μg/mg homogenates (Supplemental Figure 13, B and D). Immunostaining analysis with antibodies against PECAM-1 showed no difference in PECAM-1$^+$ vessel density and length between the control virus/GFP-injected side and the contralateral side of the brain (Figure 11, B–D). However, in the *Neo*$^{GFAP\text{-}CreER}$ cortex injected with AAV-GFAP-NTN1, the vessel length and branch points were obviously reduced as compared with those of the contralateral side of the cortical brain (Figure 11, B–D), demonstrating NTN1's sufficiency to diminish the BV deficit. Furthermore, coimmunostaining analysis of Ki67 (a cell-proliferation marker) with SLC16A1 revealed that SLC16A1$^+$ venous capillary EC proliferation was attenuated by AAV-GFAP-NTN1 injection (Supplemental Figure 15, D and E).

To examine AAV-GFAP-NTN1's effect on BBB function, the 10 kDa dextran tracer assay was carried out. The 10 kDa dextran extravasation was detected on the contralateral side, but diminished on the AAV-GFAP-NTN1–injected side (ipsilateral) (Figure 11, E and F), suggesting that NTN1 expression in astrocytes could ameliorate the BBB-permeability deficit in the Neo1-KO cortex. We further examined AAV-GFAP-NTN1's effect on desmin$^+$ pericytes, laminin-γ1$^+$ vBMs, and PLVAP$^+$ EC fenestrae in the *Neo*$^{GFAP\text{-}CreER}$ cortex. The desmin$^+$ pericytes and laminin-γ1$^+$ BVs appeared to be comparable in the ipsilateral (AAV-GFAP-NTN1 injected) and the contralateral side of the Neo1-KO cortex (Supplemental Figure 14), suggesting little effect of NTN1. However, the PLVAP$^+$ EC fenestrae were reduced by AAV-GFAP-NTN1 injection (Figure 11, G and H), suggesting a partial restoration of BBB function by NTN1. In addition to venous capillary, arterioles were examined in the mutant cortex in response to AAV-GFAP-NTN1. No obvious change in SMA$^+$ arterioles was detected upon AAV-GFAP-NTN1 injection (Supplemental Figure 15, F and G), suggesting little to no role of NTN1 in regulating arteriole diameter.

Finally, we examined NTN1's function in astrocyte distribution in the *Neo*$^{GFAP\text{-}CreER}$*;Ai9* cortex. Control AAV and AAV-GFAP-NTN1 were injected into the left cortical brain of *Neo*$^{GFAP\text{-}CreER}$*;Ai9* mice (at P30). Mice were exposed to TAM at P33 and sacrificed at P60, as illustrated in Supplemental Figure 15, A–C. Many td-Tomato$^+$ astrocytes were distributed as clusters in the Neo1 mutant contralateral cortex (Supplemental Figure 15A); however, NTN1 expression reduced the clustered astrocyte distribution phenotype in the Neo1 mutant cortex. Taken together, these results suggest that the reduced NTN1 in Neo1-KO astrocytes is likely to be responsible for the phenotypes of increased BV density, reduced BBB function, and altered astrocyte distribution.

Requirement of astrocytic NTN1 for cortical BV homeostasis and function in mouse cortex. To further investigate astrocytic NTN1's function in cortex BV/BBB maintenance, we generated *NTN1*$^{GFAP\text{-}CreER}$ mice by crossing *NTN1*$^{fl/fl}$ with *GFAP-CreER* mice. As illustrated in Figure 12A, the control (*NTN1*$^{fl/fl}$ mice) and *NTN1*$^{GFAP\text{-}CreER}$ mice were treated with TAM at P30, tail injected with dextran at P60, and sacrificed 30 minutes after dextran injection. NTN1 mRNA and protein expression were significantly reduced in the *NTN1*$^{GFAP\text{-}CreER}$ cortex exposed to TAM for 4 consecutive days (Supplemental Figure 16, A–C). Remarkably, BV/BBB deficits in the *NTN1*$^{GFAP\text{-}CreER}$ cortex that were similar to those in the *Neo*$^{GFAP\text{-}CreER}$ cortex were detected, including increase of PECAM-1$^+$ BVs (Figure 12, B and C), leaky BBB (Figure 12, B and D), elevation of EC proliferation and caveolin1$^+$ caveolae (Figure 12, E–H), and decrease of PDGFRβ$^+$ or desmin$^+$ pericytes (Figure 12, I and K, and Supplemental Figure 16, D and E) and laminin-α5$^+$ vBMs (Figure 12, J and L). Taken together, these results suggest that astrocytic NTN1, as that of NEO1, is necessary for BV/BBB homeostasis and function (Figure 12M).

Discussion

Astrocytes are known to play multiple functions in the brain, including BV homeostasis. However, the detailed mechanisms underlying astrocyte regulation of BVs/BBBs remain elusive. Here, we provide evidence that NEO1 in astrocytes is necessary for BV homeostasis and function in young adult mouse cortex. This effect appears to be cortex specific. A working hypothesis is depicted in Figure 12M, in which NEO1 promotes BMP2-induced NTN1 expression in cortical astrocytes, which regulates BV homeostasis and function. These results uncover a pathway of astrocytic NEO1 to NTN1 in promoting not only BV homeostasis, but also astrocytic distribution, and reveal a mechanism underlying astrocyte regulation of cortical BV/BBB function.

NEO1 is initially identified as a DCC family NTN receptor (14). However, its function in the NTN1 signaling pathway remains elusive because Neo1 mutant mice don't show an obvious axonal pathfinding phenotype that is detected in NTN1-deficient mice (15, 16). Alternatively, NEO1, but not DCC, is found to be a receptor for 16 repulsive guidance molecules (RGMs) modulating the BMP signaling pathways (19). In the brain, NEO1 in NSCs promotes BMP-regulated cortical astrogliogenesis (19) as well as sonic hedgehog–regulated hippocampal neurogenesis (20). Additionally, NEO1 plays important roles in fissure formation in the developing brain (42) and in preventing hydrocephalus-like deficit (17). In this paper, we provide evidence for astrocytic NEO1 in promoting BV homeostasis in the cortical brain (Figure 1). Neo1 KO in astrocytes resulted in more abundant malfunctional BVs,

which were accompanied by disrupted vBMs, reduced vascular pericytes, and impaired BBB integrity (Figure 2, Figure 3, Figure 4, and Figure 5). This function of NEO1 is cortical brain specific, as BVs in the mutant hippocampus appeared to be normal (Supplemental Figure 2), corroborating with NEO1 promotion of BMP-induced cortical, but not hippocampal, astrogliogenesis (19) and NTN1 expression (Figure 9, E–K). These results suggest that astrocytic NEO1 may regulate NTN1 expression in a brain region–specific manner, which may underlie its brain region–specific regulation of BVs/BBBs.

Arteries in the Neo1-KO cortex appeared to be thinner than those of controls (Figure 5, F and H), which may underlie the reduced blood flow in the mutant cortex. This phenotype was not rescued by expression of NTN1 (Supplemental Figure 15, F and G), suggesting an additional mechanism or mechanisms that may underlie this event. We speculate that multiple mechanisms may underlie this event. It is possible that anesthesia-induced abnormal BV blockage or contraction may cause the thinner arteries or reduced blood flow. It is also possible that impairments in astrocyte-mediated dilation of the BVs may occur in Neo1-KO mice. Interestingly, reduced Kir4.1/AQP4 and glutamate uptake and increased PGE2 synthesis and signaling in astrocytes could result in elevated vessel/smooth muscle constriction (43). In fact, AQP4 is reduced in Neo1 mutant mice (Supplemental Figure 4). Thus, it would be of interest to further investigate whether Neo1-KO astrocytes show alterations in glutamate uptake and PGE2 synthesis and signaling.

A study by Kubotera et al. (6) showed that specific ablation of astrocytes' endfeet by high-energy laser had little to no effect on BBB function within 6 hours after injury. This study is not contradictory to our study because the studies use different experiments. The astrocyte endfeet regeneration response to the laser injury (described by Kubotera et al.) is an acute response (within a few days), and the deficits in BVs/BBBs in astrocytic Neo1 KO cortex in our paper appear to be chronic events (P30 [i.p. TAM to KO Neo1] and P60 [sacrifice to examine vessel phenotypes]). In addition, the laser ablation of the endfeet acts as local and direct damage on an astrocyte-vessel interaction site, while astrocytic Neo1 KO has wider and indirect effects on vessels/BBBs due to altered secreted factors from astrocytes.

Several lines of evidence suggest that astrocyte-derived NTN1 is a key factor underlying NEO1 regulation of BV remodeling and homeostasis in mouse cortex. First, NTN1 is expressed in astrocytes in the young adult mouse cortex. Both NTN1 transcripts and proteins were detected in cultured astrocytes, and NTN1's mRNAs were detected in td-Tomato$^+$ astrocytes in *GFAP-CreER;Ai9* cortical brain sections (Figure 9). Second, astrocytic NTN1 expression was induced by BMP2 signaling in the brain region (cortex) and NEO1-dependent manners (Figure 9, G and H). Third, NTN1 was sufficient to attenuate deficits in BVs/BBBs due to astrocytic Neo1 KO in cultures and in vivo. Adding NTN1 into the CM of Neo1 KO astrocytes attenuated EC proliferation and migration (Figure 10). Expression of NTN1 into Neo1-KO astrocytes diminished the deficits in BV/BBB in the $Neo^{GFAP\text{-}CreER}$ cortex (Figure 11). Fourth, astrocytic NTN1 is necessary for BV/BBB maintenance and function, as KO NTN1 in astrocytes resulted in BV/BBB deficits in the cortex similar to those seen in Neo1-KO mice (Figure 12). Together, these observations lead to the conclusion that NTN1 is expressed in young adult cortical astrocytes, where it is upregulated by BMP-NEO1 signaling and secreted as a key extracellular protein for cortical vascular homeostasis and function. These observations also suggest that the upregulation of NTN1 expression in cortical, but not hippocampal, astrocytes by BMP-NEO1 signaling (Figure 9) may underlie NEO1's brain region–specific effect on BV homeostasis and function. However, this view requires further investigation.

In terms of the underlying mechanisms for astrocytic NEO1 to regulate BVs in a brain region–specific (cortex) manner, we suggest the following possibilities. First, astrocytic NEO1 may regulate NTN1 expression in a brain region–specific (cortex) manner. This view is supported by our results showing that cortical, but not hippocampal, Neo1-KO astrocytes show reduced NTN1 expression (Figure 9, A–F). Second, NTN1 protein distribution may be in a gradient and brain region–specific fashion, and higher concentrations of NTN1 may be in the somatosensory cortex, where it prevents hyperproliferation of tip EC cells and angiogenesis. In agreement with this view are results showing that NTN1 regulates EC proliferation in a dose-dependent manner (Figure 10). Third, in the literature, astrocyte heterogeneity (with different morphology and protein expression profiles) has been demonstrated across different brain regions. Our results suggest that the astrocyte NEO1 regulation of NTN1 may be one of the mechanisms underlying brain region–specific astrocyte heterogeneity. We hope to further test these possibilities in future experiments.

In addition to astrocytes, NTN1 is expressed in pericytes according to the single-cell RNA-Seq database (http://betsholtzlab.org/VascularSingleCells/database.html). Both the $Neo^{GFAP\text{-}CreER}$ and the $NTN1^{GFAP\text{-}CreER}$ cortex showed reductions in pericytes, which may lead to further reduction of NTN1 levels in the cortex, accelerating the cortical BV phenotype. When AAV-GFAP-NTN1 was injected into the $Neo^{GFAP\text{-}CreER}$ cortex, it failed to rescue the pericyte deficit in Neo1 mutant mice (Supplemental Figure 14), suggesting an additional mechanism or mechanisms that may underlie NEO1 regulation of pericytes. This view also requires further investigation.

NTN1 null alleles show normal BV development in embryonic stage, a critical age of angiogenesis (44). Our results demonstrate NTN1 as a key factor for BV homeostasis and function in young adults. These studies do not contradict each other, suggesting that NTN1 acts as a modulator for young adult BV homeostasis, but not an essential factor for the development of BVs. This view is also in line with literature reports showing NTN1 as a nonconventional angiogenesis factor with multiple functions (45). It inhibits tip cell–mediated sprouting angiogenesis (12, 46), promotes BBB function(47), protects ischemic injury response (48), and regulates tumor-associated angiogenesis (41). The different functions of NTN1 may depend on space, time, and NTN1 receptors. While multiple NTN1 receptors, including Unc5b, CD146, and DCC, have been implicated in NTN1-regulated angiogenesis, NEO1's function in this event remains poorly understood. Here, we propose that NEO1 not only acts as am NTN1 receptor, but also as a regulator of NTN1, promoting NTN1-mediated BV homeostasis. In addition to promoting BMP-induced NTN1 expression, the astrocytic NEO1 may act as a decoy receptor to enrich local NTN1 concentration for its role in angiogenesis. We will test this view in future experiments.

NTN1 regulates EC proliferation in a dose-dependent manner. At a high concentration (e.g., 1 μg/mL), it suppresses HUVEC proliferation and migration, while at a low concentration (10 ng/mL), it had little to no effect (Figure 10). Interestingly, under serum-starved culture conditions, such a low concentration (10 ng/mL) of NTN1 increased EC proliferation (Supplemental Figure 11), in line with the report by Park et al. (41). In addition, the observation of NTN1 suppression of EC proliferation is in line with reports that NTN1 inhibits sprouting angiogenesis via Unc5b (12, 46). Moreover, it is of interest to determine the relationship between NTN1 increase of laminin-γ1 secretion with its suppression of EC proliferation and migration and with pericyte survival and to address whether NTN1–laminin-γ1 stabilizes BVs by suppression of EC proliferation and migration and/or by prevention of pericyte apoptosis.

While several literature reports demonstrate NEO1's involvement in BMP signaling (49, 50), it has not been shown that NEO1 and BMP induce NTN1 expression. This event is cortical astrocyte specific, which may be due to differential expression of NEO1 ligands, RGMa/b, coreceptors of BMPs (51), and/or downstream proteins of phospho-$Smad_{1/5/8}$ between cortical and hippocampal astrocytes. How does BMP increase NTN1 expression in cortical astrocytes? Does the phospho-$Smad_{1/5/8}$ protein complex bind to the promoter of NTN1 and turn on its transcription? These questions remain to be addressed in future experiments. It is noteworthy that, like NTN1, BMPs also play both pro- and antiangiogenic roles in BV development, homeostasis, and remodeling (52, 53). Both BMPR1a and BMPR1b are highly expressed in astrocytes (54), and BMPR1a-KO mice show an increase in cerebral BVs with BBB leakage (55), exhibiting a BV deficit similar to that of Neo1-KO mice. These observations are in line with our model. It is also noteworthy that, in addition to NTN1 and BMPs, additional angiogenesis factors, such as VEGF, may underlie NEO1 regulation of BV/BBB homeostasis and function. In fact, VEGF transcripts were also induced in Neo1-KO astrocytes and in the mutant cortex (Figure 9, E and F, and Supplemental Figure 10). It is necessary to investigate VEGF's contribution to NEO1 mutant BV phenotypes in future experiments.

Astrocyte tiling or nonoverlapping territories between astrocytes is a prominent feature of astrocyte distribution in the brain (41). Our studies reveal another function of the astrocytic NEO1/NTN1 pathway in promoting an astrocyte tiling distribution pattern (Figure 6). The distribution deficit appears to be associated with the BV homeostasis defect, implicating a function of this event in BV/BBB maintenance. How does NTN1 regulate astrocyte distribution? Is this event due to NTN1 increase of laminin-γ1 secretion from and integrin signaling in astrocytes? These questions are of interest for future experiments.

Finally, the BV deficits detected in Neo1 mutant mice resemble to a certain degree Moyamoya disease–like vasculopathy. One of the hallmarks of Moyamoya disease is blocked blood flow with aberrant angiogenesis. The newly generated cerebral BVs in patients with Moyamoya disease are small, with dysfunctional BBB, and prone to bleeding (56). It is our hope that this study may provide insight into the etiology and therapy strategy development for Moyamoya disease.

Methods

Animals, mouse breeding, and TAM treatment. *Neogenin*$^{fl/fl}$ (*Neo*$^{fl/fl}$) mice were generated, maintained, and genotyped as described previously (20). The *hGFAP-Cre* mouse was purchased from the Jackson Laboratory (stock 004600, donated by A. Messing, University of Wisconsin, Madison, Wisconsin, USA). The cre recombinase activity in this mouse line is detectable as early as E13.5 (largely in the dorsal and medial regions of the telencephalon), and at the adult stage, it is expressed in multiple types of brain cells, including NSCs, astrocytes, oligodendroglia, ependymal cells, and neurons (21). The *GFAP-CreER*^{T2} mouse was provided by K.D. McCarthy (Department of Pharmacology, University of North Carolina, Chapel Hill, North Carolina, USA) (57). Upon TAM injection for 5 consecutive days at a young adult age (2 months), Cre activity is positive in astrocytes specifically (58). *Neo*$^{fl/fl}$ mice were crossed with *GFAP-Cre* and *GFAP-CreER*^{T2} mice to generate *Neo*$^{GFAP\text{-}Cre}$ and *Neo*$^{GFAP\text{-}CreER}$ mice, respectively. The *Ai9* mouse (from the Jackson Laboratory, stock 007909) was used as a reporter for Cre activity because it contains a loxP-flanked STOP cassette that prevents the expression of the red fluorescent protein variant (td-Tomato), and the td-Tomato in Ai9 is turned on by Cre-mediated recombination. *Ai9* mice were crossed with *Neo*$^{GFAP\text{-}CreER}$ and *GFAP-CreER*^{T2} mice to generate *Neo*$^{GFAP\text{-}CreER}$*;Ai9* and *GFAP-CreER*^{T2}*;Ai9,* respectively. *Netrin1*$^{fl/fl}$ (*Ntn1*$^{fl/fl}$) mice, also purchased from the Jackson Laboratory (stock 028038, donated by Timothy E. Kennedy, Montreal Neurological Institute, Montreal, Quebec, Canada, ref. 59), were crossed with *GFAP-CreERT2* mice to generate the Ntn1GFAP-CreER mouse line. Tg (Slc1a2-EGFP), also called Tg (GLT-1-EGFP), was obtained from the Mutant Mouse Resource and Research Center (MMRRC) (stock 010540-UCD). Nex-Cre (also called NeuroD6-Cre) mice were provided by Klaus-Armin Nave (Max-Planck-Institute of Experimental Medicine, Goettingen, Germany) (28) and crossed with Neo$^{fl/fl}$ mice to generate NeoNex-Cre.

For *Neo*$^{GFAP\text{-}CreER}$, *GFAP-CreER*^{T2}, *Neo*$^{GFAP\text{-}CreER}$*;Ai9*, *GFAP-CreER*^{T2}*;Ai9*, and *Ntn1*$^{GFAP\text{-}CreER}$ mice, TAM (MilliporeSigma) at a dose of 100 mg/kg/d was injected i.p. into the mice at P30 (for 4 consecutive days) to induce Cre recombination.

All the mouse lines indicated above were maintained on a *C57BL/6* strain background for more than 6 generations. To exclude sex as a potential confounding factor, male mice were use throughout all the experiments.

DiI perfusion. DiI (D-282, Invitrogen/Molecular Probes) perfusion was carried out according to the protocol described by Li et al. (23). In brief, DiI working solution was made by mixing 200 μl DiI stock solution (100 mg of DiI crystal in 16.7 mL of 100% ethanol and filtered with 0.45μm filter) with 10 mL of diluent (PBS with 5% glucose at a ratio of 1:4) immediately before perfusion. Mice were anesthetized by isoflurane (3%) and perfused by injections of 2 mL PBS first, then 5–10 mL of the DiI working solution, followed by 5–10 mL of the fixative buffer (4% PFA in PBS) at a rate of 1–2 mL per minute. After perfusion, mouse brain was isolated and post-fixed with 4% PFA for 3 hours. Brain samples were sectioned with the Leica Vibratome System into slices for further immunohistochemical staining analyses.

Measurement of blood flow in mouse cortex by laser Doppler. In brief, the control and *Neo*$^{GFAP\text{-}CreER}$ mice were anesthetized and their skull skins (~1.76 cm^2 area) were opened for laser Doppler scan (Moor LDI2), with a scanning depth of 1 mm. Mouse skull thickness is

approximately 150-250 μm (60), and the thickness in approximately L1–L4 cortex layers is approximately 800 μm (61). Thus, the blood flow in cortex can be measured by laser Doppler imaging analysis.

Tracer (EB and dextran) and EdU injections. To assess BBB function, EB (MilliporeSigma), 10 kDa FITC-dextran, or 70 kDa FITC-dextran (Thermo Fisher, D3305, D1821, D1823, respectively) was injected into tail veins of live mice. In brief, each mouse was put into a 50 mL tube with a hole in the middle of the tube cover, leaving its tail outside of the tube. The tracer (0.2 mg/kg in PBS) was injected into its tail vein. Thirty minutes after the injection, the mouse was anesthetized by isoflurane (3%) perfused with 4% PFA and sacrificed as described above. Its brain sample was post-fixed with 1% PFA overnight and then sectioned using the Leica Vibratome System into 50 μm thick slices. Six slices, ranging from the forebrain to the hindbrain with an interval of 500 μm, were collected for immunostaining analysis.

For EdU injection, EdU (MilliporeSigma) in phosphatase solution buffer was i.p. injected into a mouse (10 μg/g body weight, 4 times with 3-hour interval in 1 day) and the mouse was sacrificed 24 hours after the first injection. Its brain sections were stained for EdU using the iClick EU Andy Fluor 488 Imaging Kit (GeneCopoeia) following the manufacturer's instructions.

EM analysis. Electron microscopic studies were carried as described previously (62). Briefly, mice were sacrificed and perfused with 2% glutaraldehyde/2% PFA in 0.1 M phosphate buffer (pH 7.4), and their brain samples were removed and post-fixed overnight at 4°C. Somatosensory cortices were excised and post-fixed in 2% osmium tetroxide in NaCac, stained with 2% uranyl acetate, dehydrated with graded ethanol, and embedded with epon-araldite resin. Ultrathin sections were prepared using a Leica EM UC6 Ultramicrotome (Leica Microsystems) and stained with uranyl acetate and lead citrate. Prepared sections were examined by a JEM 1230 transmission EM (JEOL) at 110 kV with an UltraScan 4000 CCD camera and First Light Digital Camera Controller (Gatan). Twenty EM images per mouse were randomly picked and analyzed by investigators unaware of genotypes.

Antibody array. The antibody array kit, which contained 24 factors critical for angiogenesis (including growth factors, cytokines, chemokines, and NTN1 and NTN4) was purchased from the RayBiotech Company. The CM of primary cultured astrocytes from $Neo^{GFAP\text{-}Cre}$ and control mice was obtained under serum-starved culture conditions (DMEM). The nitrocellulose containing 24 different antibodies was incubated with the CM at 4°C overnight, washed, and subjected to further detection by reaction with HRP-streptavidin, according to the manufacturer's instructions. Fresh DMEM medium was used as a blank control.

Statistics. The number of animals varied per experiment and is noted in the corresponding figure legend. For immunohistochemical analyses, 6 or more brain sections/animal and 3 mice were evaluated (50 μm sections unless otherwise noted; every fourth or sixth section was used). Statistical analyses were performed using Prism 7 (GraphPad Software). All values are expressed as mean ± SEM. Both Student's *t* test and the Mann-Whitney *U* statistical test were used for dual comparisons. The normally distributed data were analyzed by ANOVA followed by Bonferroni's or Fisher's least significant difference post hoc tests. The exact *P* value for each analysis is indicated in the corresponding figure or figure legend. $P < 0.05$ was considered significant.

Study approval. All animal studies were approved by the Institutional Animal Care and Use Committee of Case Western Reserve University.

Immunostaining analysis, cell culture, EB measurement, RT-PCR, FISH, RNA-scope–based in situ hybridization, and adeno-associated virus (AAV) generation and injection are described in Supplemental Methods.

Author contributions

LLY, JXH, and QL designed and performed experiments and data analyses. DL, XR, JSZ, DS, and HSZ performed experiments. DL assisted with data analyses and figure organization. YGW, LM, and WCX supervised the experiments and assisted with data analyses. LLY and WCX wrote the manuscript.

Acknowledgments

We thank members of the Xiong and Mei laboratories for helpful discussions and suggestions. This work is supported in part by the start-up fund from Case Western Reserve University and the NIH (AG045781) (to WCX). We wish to thank the Electron Microscopy/Histology Core Facility in the Department of Cellular Biology and Anatomy, Medical College of Georgia, Augusta University, for EM imaging.

Address correspondence to: Wen-Cheng Xiong, 2210 Circle Robbins Building, E722, Cleveland, Ohio, 44106, USA. Phone: 216.368.4865; Email: Wen-Cheng.Xiong@case.edu.

1. Bennett RE, et al. Tau induces blood vessel abnormalities and angiogenesis-related gene expression in P301L transgenic mice and human Alzheimer's disease. *Proc Natl Acad Sci USA*. 2018;115(6):E1289–E1298.
2. Chappell JC, Wiley DM, Bautch VL. How blood vessel networks are made and measured. *Cells Tissues Organs (Print)*. 2012;195(1-2):94–107.
3. Obermeier B, Daneman R, Ransohoff RM. Development, maintenance and disruption of the blood-brain barrier. *Nat Med*. 2013;19(12):1584–1596.
4. James JM, Mukouyama YS. Neuronal action on the developing blood vessel pattern. *Semin Cell Dev Biol*. 2011;22(9):1019–1027.
5. Mishra A. Binaural blood flow control by astrocytes: listening to synapses and the vasculature. *J Physiol (Lond)*. 2017;595(6):1885–1902.
6. Kubotera H, Ikeshima-Kataoka H, Hatashita Y, Allegra Mascaro AL, Pavone FS, Inoue T. Astrocytic endfeet re-cover blood vessels after removal by laser ablation. *Sci Rep*. 2019;9(1):1263.
7. Eichmann A, Thomas JL. Molecular parallels between neural and vascular development. *Cold Spring Harb Perspect Med*. 2013;3(1):a006551.
8. Adams RH, Eichmann A. Axon guidance molecules in vascular patterning. *Cold Spring Harb Perspect Biol*. 2010;2(5):a001875.
9. Wälchli T, et al. Wiring the vascular network with neural cues: a CNS perspective. *Neuron*. 2015;87(2):271–296.
10. Tu T, et al. CD146 acts as a novel receptor for netrin-1 in promoting angiogenesis and vascular development. *Cell Res*. 2015;25(3):275–287.
11. Bouvrée K, et al. Netrin-1 inhibits sprouting angiogenesis in developing avian embryos. *Dev Biol*. 2008;318(1):172–183.
12. Lu X, et al. The netrin receptor UNC5B mediates guidance events controlling morphogenesis of the vascular system. *Nature*. 2004;432(7014):179–186.
13. Srivatsa S, et al. Unc5C and DCC act downstream of Ctip2 and Satb2 and contribute to corpus callosum formation. *Nat Commun*. 2014;5:3708.
14. Xu K, et al. Neural migration. Structures of netrin-1 bound to two receptors provide insight into its axon guidance mechanism. *Science*. 2014;344(6189):1275–1279.
15. Huang Z, Xiong WC. Neogenin-YAP signaling in neocortical astrocytic differentiation. *Neurogenesis (Austin)*. 2016;3(1):e1248735.

16. Hakanen J, Salminen M. Defects in neural guidepost structures and failure to remove leptomeningeal cells from the septal midline behind the interhemispheric fusion defects in Netrin1 deficient mice. *Int J Dev Neurosci*. 2015;47(Pt B):206–215.
17. O'Leary CJ, et al. Neogenin recruitment of the WAVE regulatory complex to ependymal and radial progenitor adherens junctions prevents hydrocephalus. *Cell Rep*. 2017;20(2):370–383.
18. Murase S, Horwitz AF. Deleted in colorectal carcinoma and differentially expressed integrins mediate the directional migration of neural precursors in the rostral migratory stream. *J Neurosci*. 2002;22(9):3568–3579.
19. Huang Z, et al. Neogenin promotes BMP2 activation of YAP and Smad1 and enhances astrocytic differentiation in developing mouse neocortex. *J Neurosci*. 2016;36(21):5833–5849.
20. Sun D, et al. Neogenin, a regulator of adult hippocampal neurogenesis, prevents depressive-like behavior. *Cell Death Dis*. 2018;9(1):8.
21. Zhuo L, Theis M, Alvarez-Maya I, Brenner M, Willecke K, Messing A. hGFAP-cre transgenic mice for manipulation of glial and neuronal function in vivo. *Genesis*. 2001;31(2):85–94.
22. Doetsch F. The glial identity of neural stem cells. *Nat Neurosci*. 2003;6(11):1127–1134.
23. Li Y, Song Y, Zhao L, Gaidosh G, Laties AM, Wen R. Direct labeling and visualization of blood vessels with lipophilic carbocyanine dye DiI. *Nat Protoc*. 2008;3(11):1703–1708.
24. Stockinger H, et al. Molecular characterization and functional analysis of the leukocyte surface protein CD31. *J Immunol*. 1990;145(11):3889–3897.
25. Bradford D, Faull RL, Curtis MA, Cooper HM. Characterization of the netrin/RGMa receptor neogenin in neurogenic regions of the mouse and human adult forebrain. *J Comp Neurol*. 2010;518(16):3237–3253.
26. Andrusiak MG, et al. Rb/E2F regulates expression of neogenin during neuronal migration. *Mol Cell Biol*. 2011;31(2):238–247.
27. Garcia AD, Doan NB, Imura T, Bush TG, Sofroniew MV. GFAP-expressing progenitors are the principal source of constitutive neurogenesis in adult mouse forebrain. *Nat Neurosci*. 2004;7(11):1233–1241.
28. Goebbels S, Bormuth I, Bode U, Hermanson O, Schwab MH, Nave KA. Genetic targeting of principal neurons in neocortex and hippocampus of NEX-Cre mice. *Genesis*. 2006;44(12):611–621.
29. Daneman R, Prat A. The blood-brain barrier. *Cold Spring Harb Perspect Biol*. 2015;7(1):a020412.
30. Smyth LCD, et al. Markers for human brain pericytes and smooth muscle cells. *J Chem Neuroanat*. 2018;92:48–60.
31. Tkachenko E, et al. Caveolae, fenestrae and transendothelial channels retain PV1 on the surface of endothelial cells. *PLoS ONE*. 2012;7(3):e32655.
32. Abbott NJ, Patabendige AA, Dolman DE, Yusof SR, Begley DJ. Structure and function of the blood-brain barrier. *Neurobiol Dis*. 2010;37(1):13–25.
33. Vanlandewijck M, et al. A molecular atlas of cell types and zonation in the brain vasculature. *Nature*. 2018;554(7693):475–480.
34. Madisen L, et al. A robust and high-throughput Cre reporting and characterization system for the whole mouse brain. *Nat Neurosci*. 2010;13(1):133–140.
35. Chung WS, Allen NJ, Eroglu C. Astrocytes control synapse formation, function, and elimination. *Cold Spring Harb Perspect Biol*. 2015;7(9):a020370.
36. Kalna V, et al. The transcription factor ERG regulates super-enhancers associated with an endothelial-specific gene expression program. *Circ Res*. 2019;124(9):1337–1349.
37. Lamalice L, Le Boeuf F, Huot J. Endothelial cell migration during angiogenesis. *Circ Res*. 2007;100(6):782–794.
38. Preisinger C, et al. YSK1 is activated by the Golgi matrix protein GM130 and plays a role in cell migration through its substrate 14-3-3zeta. *J Cell Biol*. 2004;164(7):1009–1020.
39. Reed MJ, Koike T, Sadoun E, Sage EH, Puolakkainen P. Inhibition of TIMP1 enhances angiogenesis in vivo and cell migration in vitro. *Microvasc Res*. 2003;65(1):9–17.
40. Dyer LA, Pi X, Patterson C. The role of BMPs in endothelial cell function and dysfunction. *Trends Endocrinol Metab*. 2014;25(9):472–480.
41. Park KW, et al. The axonal attractant Netrin-1 is an angiogenic factor. *Proc Natl Acad Sci USA*. 2004;101(46):16210–16215.
42. Conrad S, et al. RGMb controls aggregation and migration of Neogenin-positive cells in vitro and in vivo. *Mol Cell Neurosci*. 2010;43(2):222–231.
43. Attwell D, Buchan AM, Charpak S, Lauritzen M, Macvicar BA, Newman EA. Glial and neuronal control of brain blood flow. *Nature*. 2010;468(7321):232–243.
44. Yung AR, Nishitani AM, Goodrich LV. Phenotypic analysis of mice completely lacking netrin 1. *Development*. 2015;142(21):3686–3691.
45. Castets M, Mehlen P. Netrin-1 role in angiogenesis: to be or not to be a pro-angiogenic factor? *Cell Cycle*. 2010;9(8):1466–1471.
46. Larrivée B, et al. Activation of the UNC5B receptor by Netrin-1 inhibits sprouting angiogenesis. *Genes Dev*. 2007;21(19):2433–2447.
47. Podjaski C, et al. Netrin 1 regulates blood-brain barrier function and neuroinflammation. *Brain*. 2015;138(Pt 6):1598–1612.
48. Yu J, et al. Netrin-1 ameliorates blood-brain barrier impairment secondary to ischemic stroke via the activation of PI3K pathway. *Front Neurosci*. 2017;11:700.
49. Tian C, Shi H, Xiong S, Hu F, Xiong WC, Liu J. The neogenin/DCC homolog UNC-40 promotes BMP signaling via the RGM protein DRAG-1 in C. elegans. *Development*. 2013;140(19):4070–4080.
50. Healey EG, Bishop B, Elegheert J, Bell CH, Padilla-Parra S, Siebold C. Repulsive guidance molecule is a structural bridge between neogenin and bone morphogenetic protein. *Nat Struct Mol Biol*. 2015;22(6):458–465.
51. Mueller TD. RGM co-receptors add complexity to BMP signaling. *Nat Struct Mol Biol*. 2015;22(6):439–440.
52. Benn A, Hiepen C, Osterland M, Schütte C, Zwijsen A, Knaus P. Role of bone morphogenetic proteins in sprouting angiogenesis: differential BMP receptor-dependent signaling pathways balance stalk *vs*. tip cell competence. *FASEB J*. 2017;31(11):4720–4733.
53. Icli B, et al. MicroRNA-26a regulates pathological and physiological angiogenesis by targeting BMP/SMAD1 signaling. *Circ Res*. 2013;113(11):1231–1241.
54. Sahni V, et al. BMPR1a and BMPR1b signaling exert opposing effects on gliosis after spinal cord injury. *J Neurosci*. 2010;30(5):1839–1855.
55. Araya R, et al. BMP signaling through BMPRIA in astrocytes is essential for proper cerebral angiogenesis and formation of the blood-brain-barrier. *Mol Cell Neurosci*. 2008;38(3):417–430.
56. Pollak L. Moyamoya disease and moyamoya syndrome. *N Engl J Med*. 2009;361(1):98.
57. Casper KB, Jones K, McCarthy KD. Characterization of astrocyte-specific conditional knockouts. *Genesis*. 2007;45(5):292–299.
58. Park YM, Chun H, Shin JI, Lee CJ. Astrocyte specificity and coverage of hGFAP-CreERT2 [Tg(GFAP-Cre/ERT2)13Kdmc] mouse line in various brain regions. *Exp Neurobiol*. 2018;27(6):508–525.
59. Bin JM, et al. Complete loss of Netrin-1 results in embryonic lethality and severe axon guidance defects without increased neural cell death. *Cell Rep*. 2015;12(7):1099–1106.
60. Paxinos G, Franklin KBJ, Franklin KBJ. *The mouse brain in stereotaxic coordinates*. Academic Press; 2001.
61. Constantinople CM, Bruno RM. Deep cortical layers are activated directly by thalamus. *Science*. 2013;340(6140):1591–1594.
62. Tian Y, et al. VPS35-deficiency results in an impaired AMPA receptor trafficking and decreased dendritic spine maturation. *Mol Brain*. 2015;8(1):70.